ELECTROKINETIC AND ACOUSTIC MANIPULATIONS OF COLLOIDAL AND BIOLOGICAL PARTICLES

A Dissertation

by

SEUNGKYUNG PARK

Submitted to the Office of Graduate Studies of
Texas A&M University
in partial fulfillment of the requirements for the degree of

DOCTOR OF PHILOSOPHY

December 2008

Major Subject: Mechanical Engineering

ELECTROKINETIC AND ACOUSTIC MANIPULATIONS OF COLLOIDAL AND BIOLOGICAL PARTICLES

A Dissertation

by

SEUNGKYUNG PARK

Submitted to the Office of Graduate Studies of
Texas A&M University
in partial fulfillment of the requirements for the degree of

DOCTOR OF PHILOSOPHY

Approved by:

Co-Chairs of Committee,	Ali Beskok
	Sai C. Lau
Committee Members,	Suresh D. Pillai
	Victor Ugaz
Head of Department,	Dennis O'Neal

December 2008

Major Subject: Mechanical Engineering

ABSTRACT

Electrokinetic and Acoustic Manipulations of Colloidal

and Biological Particles. (December 2008)

Seungkyung Park, B.S.; M.S., Korea Advanced Institute of Science and Technology

Co-Chairs of Advisory Committee: Dr. Ali Beskok
Dr. Sai C. Lau

Recent advances in microfluidic technologies have enabled integration of the functional units for biological and chemical analysis onto miniaturized chips, called Lab-on-a-Chip (LOC). However, the effective manipulation and control of colloidal particles suspended in fluids are still challenging tasks due to the lack of clear characterization of particle control mechanisms. The aim of this dissertation is to develop microfluidic techniques and devices for manipulating colloids and biological particles with the utilization of alternating current (AC) electric fields and acoustic waves.

The dissertation presents a simple theoretical tool for predicting the motion of colloidal particles in the presence of AC electric field. Dominant electrokinetic forces are explained as a function of the electric field conditions and material properties, and parametric experimental validations of the model are conducted with particles and biological species. Using the theoretical tool as an effective framework for designing electrokinetic systems, a dielectrophoresis (DEP) based microfluidic device for trapping bacterial spores from high conductivity media is developed. With a simple planar

electrode having well defined electric field minima that can act as the target-attachment/detection sites for integration of biosensors, negative DEP trapping of spores on patterned surfaces is successfully demonstrated. A further investigation of DEP colloidal manipulation under the effects of electrothermal flow induced by Joule heating of the applied electric field is conducted. A periodic structure of the electrothermal flow that enhances DEP trapping is numerically simulated and experimentally validated.

An acoustic method is investigated for continuous sample concentration in a microscale device. Fast formation of particle streams focused at the pressure nodes is demonstrated by using the long-range forces of the ultrasonic standing waves (USW). High frequency actuation suitable for miniaturization of devices is successfully applied and the device performance and key parameters are explained.

Further extension and integration of the technologies presented in this dissertation will enable a chip scale platform for various chemical and biological applications such as drug delivery, chemical analyses, point-of-care clinical diagnosis, biowarfare and biochemical agent detection/screening, and water quality control.

DEDICATION

This dissertation is dedicated to my wife, Minkyung, for her love and support.

ACKNOWLEDGEMENTS

I would like to thank my advisor, Professor Ali Beskok, for all his guidance and encouragement during my entire doctoral program. I am indebted to him for inspiring me many creative ideas and giving me the opportunity to work in multidisciplinary fields.

I would also like to thank my advisory committee, Professor Sai C. Lau, Professor Victor Ugaz, and Professor Suresh D. Pillai, for their invaluable comments and assistance on my dissertation.

I express my gratitude to research staffs in mechanical and chemical engineering departments for their help in micro-fabrication and measurement. Many thanks also go to aerospace engineering department at Old Dominion University for their sincere support during my stay in Norfolk.

I am also grateful to all my colleagues, Ashwin, Pradip, Ho-Jun, Bo-Hung, Bayram, Mehti, Can, Yashi, Murat, and Eren, for valuable discussions and their help.

Finally, I would like to thank to my family. This dissertation certainly would not have been possible without encouragement and support of them.

This research was supported by the U.S. Department of Homeland Security (Grant number N-00014-04-1-0659), through a grant awarded to the National Center for Food Protection and Defense at the University of Minnesota. Any opinions, findings, conclusions, or recommendations expressed in this publication are those of the author(s) and do not represent the policy or position of the Department of Homeland Security.

TABLE OF CONTENTS

Page

LIST OF FIGURES

FIGURE Page

FIGURE Page

FIGURE Page

FIGURE Page

LIST OF TABLES

1. INTRODUCTION

1.1 Microfluidics and Lab-on-a-Chip Systems

Microfluidics is the science and technology of systems that process or manipulate small amounts of fluids, using channels with dimensions of tens to hundreds of micrometers.[1] Microfluidic approaches for rapid manipulation and detection of colloids and biological particles suspended in liquid media have received enormous recent attention because of the quest for cheap portable devices able to perform simple analytical tasks on the cellular length scale.[2] The potential uses of microfluidic systems in physical science for control systems, heat management, energy generation, and display technology are the other driving forces in microfluidic research.[3]

Advancement of microfabrication technologies has enabled the integration of functional units for biochemical analysis onto miniaturized chips, and the realization of such a Lab-on-a-Chip (LOC) concept has been considered as the most important application of microfluidics. LOC systems provide analytical improvements associated with the minimized consumption of reagents, increased automation, short reaction time, and reduced manufacturing costs.[4] The demand of LOC systems has been growing rapidly due to its potentials on drug delivery, chemical analyses, point-of-care clinical devices, biowarfare and biochemical agent detection, high throughput screening, and

---

This dissertation follows the style of *Analytical Chemistry.*

water quality control.[5] Since LOC system aims miniaturization of a typical room-sized laboratory, major fluidic components for handling of analytical samples are similarly required including the pump, valve, mixer, concentrator, filter, sensor, etc. Thus, various types of microfluidic technologies are being widely investigated by many researchers for the development of key LOC components.[6-9]

Analytical samples are typically in the form of aqueous mixtures that carry cells or chemical reactants or indicators. Standard analytical operations of the samples generally require 1) sample preparation including the pre-concentration and lysis; 2) fluid and particle handling; 3) mixing and reaction; 4) separation; and 5) detection steps.[10] For each process, effective manipulation and control of colloidal particles and suspending fluids are fundamental tasks. Although many conventional devices exist in macroscale, many different physical phenomena in microscale (e.g., laminar flow with negligible inertial effects) often limit the miniaturization of them. Thus, significant efforts are spent for the development of new approaches for colloidal manipulations in a small scale device. Several mechanisms have been employed to manipulate colloidal suspensions with the application of external force fields, which commonly draw their advantages from the large surface area to volume ratio in microfluidic systems.[11] However, the development of efficient and versatile manipulation systems for colloidal particles is still a challenging task due to the lack of clear characterization of control mechanisms.

1.2 Microfluidic Manipulation Techniques

Microfluidic manipulation techniques of colloidal suspensions can be categorized based on the physical forces employed into the electromagnetic, optical, mechanical, electrokinetic and acoustic methods.[11] Some recent examples of these methods are summarized in Table 1.1. Each technique has its advantages and unique features. Electromagnetic method utilizes the force exerted on magnetic beads that are selectively attached to target species, and thus offers a clean, versatile, and non-invasive manipulation. However, it essentially requires specific methods for tagging or conjugating the target species with magnetic beads. Due to non-contact and contamination-free manipulation process, optical manipulation attracts great attention, whereas its complicated optical setup, complex operation, and expensive instrumentation limit further applications in microfluidics. Mechanical method includes size-dependent filter, grooved surface, and micro-gripper,[11] and it usually suffers from poor selectivity and complex fabrication process. Particles or suspending fluids can be manipulated by electrokinetic forces such as electrophoresis (EP), dielectrophoresis (DEP), electroosmosis (EO), and electrothermal effects. Electrokinetic methods offer many benefits including the selective control of colloidal motion and simple integration with other conventional electronic components, which will be discussed more specifically in Section 2 and 3. Meanwhile, the methods require embedded or external microelectrodes for supplying electric fields, and thus the design and fabrication of electrodes that allow sufficient spatial control of target species are important. Acoustic method also provides non-invasive manipulation energized by acoustic wave fields inside microchannels. One

Table 1.1 Examples of various types of microfluidic colloidal manipulations

Type	Method	Analytical Function	Sample	Ref.
Electrokinetic	EP plate	Capture	Bacteria	12
	DEP post	Positioning	Cell	13
Electromagnetic	Electromagnet matrix	Positioning	Bacteria	14
	Magnetophoresis	Separation	Particle	15
Acoustic	USW	Separation	Cell	89
	SAW	Positioning	Particle	16
Optical	Optical switch	Sorting	Cell	17
	Optical lattice	Separation	Cell Protein Capsule	18
Mechanical	Post Array	Separation	DNA	19

important characteristic of acoustic manipulation is that a long-range force field can be created, whereas electrokinetic/magnetic and optical methods utilize point-wise forces. Among these, two specific techniques are selected and investigated in this dissertation: electrokinetic and acoustic methods.

1.3 Objectives

The aim of this dissertation is to develop microfluidic techniques for manipulation and control of colloids and biological particles suspended in media. Emphasis is made on the understanding and characterization of colloidal motions in

presence of electric fields and acoustic waves, which can provide efficient tools for the development of LOC devices. The overall approach is to utilize electrokinetic transport mechanism to capture, pattern and separate particles from the suspending media, and to employ the long-range high throughput characteristic of acoustic forces for sample concentration. The specific objectives of this research work are:

- Understanding of alternating current (AC) electrokinetic transport of colloidal particles in a wide spectrum of electric field amplitude and frequency, and medium conductivity based on the theoretical and experimental observations of dominant transport mechanism
- Utilization of electrokinetic forces to manipulate and trap biological species directly from high conductivity media, and broadening the practical limit of electrokinetic techniques to sample separation and detection in complex food matrices and physiological fluids
- Development of a specific electrode configuration for DEP manipulation of colloidal particles and its characterization through theoretical, numerical and experimental investigations
- Demonstration of acoustic manipulation of colloidal suspensions as a promising method for high throughput sample concentration in a microfluidic device, and prediction of performance parameters

1.4 Dissertation Outline

This dissertation is organized as follows: Section 2 describes a theoretical model and its experimental validations for the motion of colloidal particles subjected to an AC electric field. A negative DEP based microfluidic device for trapping of pathogen samples from complex food matrices is presented in Section 3. Numerical and experimental investigation of electrothermal effects on the DEP manipulation is performed in section 4. Section 5 demonstrates a sample concentration method based on ultrasonic standing wave (USW). A summary of conclusions and future research are provided in Section 6.

2. ALTERNATING CURRENT ELECTROKINETIC MOTION OF COLLOIDAL PARTICLES : SCALING ANALYSIS*

2.1 Introduction

With the advancement of microfabrication methods, AC electrokinetic techniques such as electrophoresis (EP), dielectrophoresis (DEP) and AC electroosmosis (AC-EO) have been widely investigated and utilized for separating, sorting, mixing, and detection of colloidal particles and biological species on microscale devices.[20-27] Alternating current electrokinetic techniques provide a great potential for development of micro total analysis systems (μ-TAS). Because colloidal motion is mainly induced by interaction with an AC electric field, manipulation of submicrometer scale particles without mechanical moving parts is possible, and the direction and magnitude of the colloidal motion can be controlled by adjusting the frequency and amplitude of the applied electric field.[28] Moreover, AC electrokinetic techniques are well suited for integration with other electronic components on a single chip with a small foot print area.[29] However, AC electrokinetic manipulation of colloidal particles is generally limited by the applicable electric field conditions and relative polarizability of the suspending medium compared to that of the particles and electrodes. Accordingly, the design and optimization process of AC electrokinetic devices require performance

prediction and validation over specific operational ranges of the electric field, which should be considered as a function of the electrode geometry, and electromechanical properties of the target species and suspending medium. For example, when the size and properties of the target species are fixed, DEP forces can be represented as a function of the ionic strength of media, electric field frequency and amplitude, and the electrode geometry. In order to utilize DEP for manipulating colloidal particles, the magnitude of the DEP force should be large enough to dominate other forces. If this is induced using large electric fields, electrolysis of the suspending medium can occur.[30] Relative polarizability of the suspending medium can be controlled by adjusting the molarity of the buffer solution to vary the direction and magnitude of DEP at certain frequency ranges. However, high conductivity media often causes undesirable electrothermal effects.[31] It should be also noted that selection of the buffer conductivity is restrictive in the case of biological samples, because excessive osmotic stress can cause cell damage.[32] Thus, design and development of devices for specific applications require characterization of each AC electrokinetic mechanism over the desired range of electric field strength and buffer concentration.

Alternating current electrokinetic forces and resultant motion of colloidal particles suspended in an aqueous medium have been investigated by many researchers to develop microfluidic devices for various applications. Approximate analytical series solutions to predict DEP forces exerted on colloidal particles are demonstrated in the case of the simple interdigitated electrode system, using Green's functions[33] and Fourier series.[34] However, numerical simulation would be the most common method to analyze

electric field and the electrokinetic forces induced by complex electrode geometries. Numerous results of detailed numerical simulations of microconcentrators, particle sorters and separators, mixers, and biosensors that utilize DEP and AC-EO are available in the literature.[35-39] Numerical simulations require intensive computations, especially for the performance optimization process that considers variations in the electric field conditions and the device geometries. For device applications, it is important to figure out the basic constraints of electrokinetic manipulation and appropriate operating conditions for target species in the early design stages. Thus, efficient methods to describe the relationship between the applicable electric field conditions and AC electrokinetic transport of colloidal particles are required.

Castellanos et al.[40] presented a scaling analysis of particle dynamics and a summary of the type of fluid flow observed in a simplified system consisting of interdigitated electrodes, whereas Bahukudumbi et al.[41] have shown modified scaling analysis in terms of electrokinetic velocities. The simple scaling law of electrokinetic forces with respect to system parameters was demonstrated as an effective tool for the prediction of the dominant transport mechanism without numerical calculations. However, different types of DEP (negative/positive DEP) and the variation of the DEP force magnitude were not represented effectively in previous studies, because the colloidal particle's relative polarizability was not taken into account. For electrokinetic applications, different strategies are generally required for designing electric fields and devices as DEP characteristics change as a function of the relative polarizability of particles. Particles are attracted toward the electrodes' edges for positive DEP, whereas

negative DEP repels particles from the electrode surface. On the basis of the direction of the DEP force, the motion of colloidal particles can be induced in a specific direction by creating electric field maxima or minima at desired locations. Relative polarizability of the particle is a function of the material properties, electric field frequency, and conductivity of the suspending medium. Thus, specific DEP manipulation of colloidal particles should be considered within a limited range of electric field frequency and conductivity of the buffer solution. Relative polarizability of the buffer solution with respect to the electrodes is also important, because AC-EO and EP are restricted by the double layer polarization on the electrodes. Hence, a simple and reliable theoretical tool, which can effectively consider the polarizability variations and predict the resultant particle motion, is required to design and optimize AC electrokinetic devices.

In this section, we demonstrate an effective way of predicting the AC electrokinetic motion of colloidal particles in a microscale device. A modified scaling analysis is constructed by considering the relative magnitudes of AC electrokinetic motion (EP, DEP and AC-EO) and Brownian motion of colloidal particles on interdigitated microelectrodes, which have simple planar geometry and analytically obtained electric field. Dominant transport mechanisms at a given electric field and material conditions are described using phase diagrams, and effects of a particle's relative polarizability and the ionic concentration of buffer solution are explained. Then, the results are validated through parametric experiments for different kinds of colloidal particles (polymeric and metallic particles and biological species) at various electric field conditions. Dominant transport mechanisms of each particle with different polarization

characteristics are observed and compared with the results of the scaling analysis. As a result, we have shown that the theoretical model can provide quantifiable information for AC electrokinetic motion of colloidal particles over broad ranges of electric field frequencies and amplitudes.

2.2 Methods and Materials

Interdigitated gold electrodes with 30 μm spacing were deposited on microscope slides using conventional photolithographic techniques. A circular flow chamber (10 mm diameter) was constructed by placing a 1 mm thick O-ring spacer on the observation area, and it was covered with a microscope cover glass during the experiments. Three different samples were prepared with polystyrene and gold particles and Clostridium sporogenes bacterial spore (ATCC 3584). Fluorescent polystyrene particles of 1 μm (FluoSpheres, Interfacial Dynamics) were diluted with distilled water, which has a conductivity of 2.6×10^{-3} S/m measured via a conductivity meter (PHH-80MS, Omega). The particle concentration was adjusted to 1×10^{8}/mL approximately from a manufacturer's solution. Gold particles of 800 nm (Bangs Laboratories) were diluted with deionized (DI) water (Simplicity, Millipore), and the ionic concentration of the solution was adjusted by adding 0.1 mM $NaHCO_3$. Stained C. sporogenes sample was prepared as described in Appendix section and was diluted with DI water to obtain a concentration of $\sim 10^{7}$ spores/mL. Test solutions were then pippeted into the fluid chamber, and AC voltage up to 10 V peak-to-peak was supplied by a function generator (AFG 3102, Tektronix) in the frequency range of 0~100 MHz. Particle motion was

observed using an optical microscope (TE2000-U, Nikon) and a 10X objective (0.3 NA). Images were captured using software (Insight, TSI) and a CCD camera (PowerView1.4MP, TSI) with 1376 × 1040 pixel resolution (6.45 μm pixel size).

2.3 Results and Discussion

2.3.1 Scaling Analysis

In the presence of a non-uniform AC electric field, colloidal particles suspended in an aqueous medium experience electrokinetic forces including EP, DEP, and hydrodynamic drag force due to the bulk fluid motion induced by AC-EO at a certain frequency range. In addition to electrical forces, the particles are also influenced by Brownian motion. Lateral motion of colloidal particle motion is generally driven by interaction of these forces, and precise analysis for each transport mechanism is required for manipulation of particles in microfluidic devices. To reduce the effort involved in detailed numerical simulations and to gain understanding for the order of magnitude of each transport mechanism, we developed a scaling analysis that predicts dominant forces in a microscale device based on the maximum displacement of colloidal particles on interdigitated microelectrodes. The scaling map results in prediction of the dominant transport mechanism at a given operational condition. It also enables production of phase diagrams that describe particle motion as functions of the electric field frequency, amplitude and media conductivity.

2.3.2 Alternating Current Electroosmosis

For coplanar parallel electrodes, shown in Figure 2.1, electric field distortion due to the top surface of the fluid chamber is negligible if the electrolyte is confined in a tall fluid chamber of height much greater than several electrode width and spacing. Then, the electric field between two electrodes can be assumed as half-circular lines near the electrode surface. The electrokinetic forces can be represented in simple analytical forms using this simplified electric field distribution. The fluid motion on interdigitated electrodes due to AC-EO was previously explained in a series of papers.[42-44] The tangential AC electric field produces electroosmotic fluid velocity due to the potential drop across the double layer on the electrodes, which can be represented as[44]

$$u_{EO} = \frac{\varepsilon\varepsilon_0}{\eta}\Delta\phi_D E_t = -\frac{\varepsilon\varepsilon_0}{4\eta}\Lambda\frac{\partial}{\partial r}\left(\left|\Delta\phi_{DL}\right|^2\right), \tag{2.1}$$

where ε_0 and ε are the absolute permittivity and relative permittivity of the medium respectively, η is the viscosity, $\Delta\phi_D$ and $\Delta\phi_{DL}$ are the potential drop across the diffuse layer and the double layer respectively, and E_t is the tangential electric field. The capacitance ratio Λ is given by, $\Lambda = C_S/(C_S+C_D)$, where C_S is the capacitance of the Stern layer, and C_D is the capacitance of the diffuse layer. C_S=0.007 F/m^2 is used based on the experimental result of impedance measurements.[44] With expressions for resistance of the fluid and capacitance of the double layer, electric circuit analogy can be applied to model the double layer potential drop by[45, 46]

$$\Delta\phi_{DL} = \frac{V_0}{2(1+j\Omega)}, \tag{2.2}$$

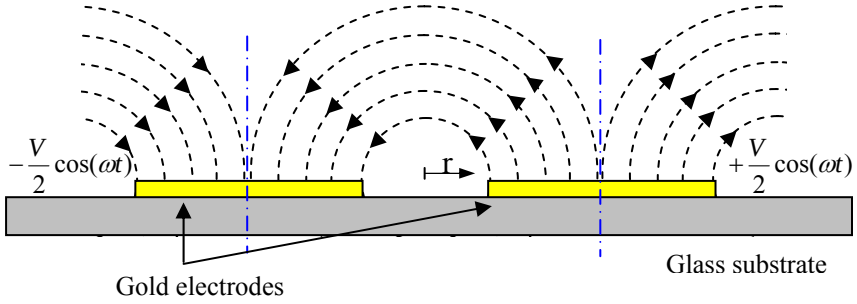

Figure 2.1 Schematics of simplified electric field lines on interdigitated electrodes.

where V_0 is the applied voltage, $j=\sqrt{-1}$, $\Omega=\Lambda\omega\varepsilon\varepsilon_0\pi r/2\sigma\lambda_D$, ω is the radian frequency, σ is the conductivity of the fluid, and λ_D is the Debye length. Then, the resultant displacement due to AC-EO motion can be expressed as[40]

$$X_{AC-EO} = \frac{1}{8}\Lambda\frac{\varepsilon\varepsilon_0 V_0^{\,2}}{\eta r}\frac{\Omega^2}{(1+\Omega^2)^2}t\,. \tag{2.3}$$

Alternating current electroosmotic displacement becomes zero as the non-dimensional frequency Ω goes to zero or infinity, which represents a bell shaped function with both ends approaching zero.

2.3.3 Dielectrophoresis

In the case of an electric field with constant phase, the time-averaged DEP force can be represented as[47]

$$F_{DEP} = 2\pi\varepsilon\varepsilon_0 a^3\,\mathrm{Re}\{K\}\nabla\left|E\right|^2, \tag{2.4}$$

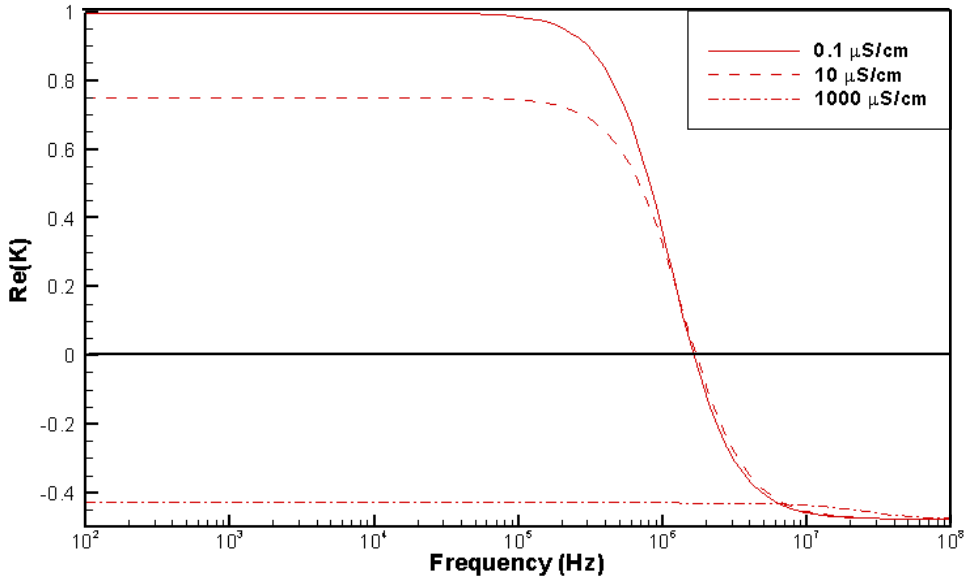

Figure 2.2 Plot of the real part of the Clausius-Mossotti factor for a solid spherical dielectric particle at various medium conductivities (for ε_p=2.5, σ_p=0.01 S/m, and ε=78).

where a is the particle radius, E is the electric field, and K is the Clausius-Mossotti (CM) factor. For homogeneous particles suspended in a medium, the CM factor is given by

$$K(\varepsilon_p^*, \varepsilon^*) = \frac{\varepsilon_p^* - \varepsilon^*}{\varepsilon_p^* + 2\varepsilon^*}, \tag{2.5}$$

where ε^* is the complex electric permittivity of the media, which can be represented as $\varepsilon^*=\varepsilon-j\sigma/\omega$. Subscript p refers to the particle. The CM factor represents the effective polarizability of the particle with respect to the suspending medium, which is a strong function of the applied frequency. The value of $\mathrm{Re}\{K\}$ varies between +1 and −1/2. With dependence on the sign of $\mathrm{Re}\{K\}$, particle motion is induced toward the electrode

surface (positive DEP) or away from the electrodes (negative DEP). Figure 2.2 shows the variation of $\mathrm{Re}\{K\}$ as a function of the electric field frequency and ionic strength of the suspending medium for solid spherical dielectric particles with the parameters ε_p=2.55, ε=78.5, and σ_p=0.01 S/m. The sign of $\mathrm{Re}\{K\}$ is switched from positive to negative around the crossover frequency (~2 MHz) for low conductivity buffer solution cases (10^{-5} S/m and 10^{-4} S/m). However, only negative $\mathrm{Re}\{K\}$ is observed in the whole frequency range for the high conductivity buffer case (10^{-1} S/m), which shows a limitation of positive DEP by the conductivity of the buffer solution. Because the DEP force is proportional to the gradient of the electric field, a small device scale and high operational voltage are required to amplify the DEP motion of the suspended particles. Because of the potential loss induced by electrode polarization, the actual potential supplied to the fluid can be expressed as[46]

$$V_{fluid} = V_0 - 2\Delta\phi_{DL} = V_0 \frac{j\Omega}{1 + j\Omega}. \tag{2.6}$$

With the utilization of the half circular electric field approximation ($E=V_{fluid}/\pi r$) and assuming force balance with Stokes drag for small particles, characteristic DEP displacement can be represented as[40]

$$X_{DEP} = \frac{1}{3\pi^2}\mathrm{Re}\{K\}\frac{a^2\varepsilon\varepsilon_0}{\eta}\frac{\beta^2 V_0^{\,2}}{r^3}t, \tag{2.7}$$

where $\beta^2=\Omega^2/(1+\Omega^2)$. It can be observed that β goes to unity as Ω approaches infinity, and thus the effect of electrode polarization can be neglected for large Ω.

2.3.4 Electrophoresis

For thin electrical double layers ($a/\lambda_D >> 1$), dynamic mobility of spherical particles can be expressed as[48]

$$\mu_d = \frac{\varepsilon\varepsilon_0\zeta_p}{\eta} G\left(\frac{\omega a^2}{\nu}\right), \tag{2.8}$$

where ζ_p is the zeta potential of the particle, ν is the kinematic viscosity, and G is a function that represents inertial effects of particle motion as a function of the Womersley number $\alpha = a\sqrt{\omega/\nu}$, and is given as[48]

$$G(\alpha^2) = \frac{1+(1+j)\alpha/\sqrt{2}}{1+(1+j)\alpha/\sqrt{2}+j(\alpha^2/9)\left(3+(\rho_p-\rho)/\rho\right)}, \tag{2.9}$$

where ρ_p and ρ are the density of the particle and medium, respectively. Electrophoretic displacement can be derived from particle velocity ($u_{EP}=\mu_d E$) as

$$X_{EP} = \frac{\varepsilon\varepsilon_0\zeta_p}{\eta} G\left(\frac{\omega a^2}{\nu}\right)\left(\frac{\beta V_0}{\pi r}\right)\frac{1}{\omega}\sin(\omega t), \tag{2.10}$$

where ($\beta V_0/\pi r$) is an approximation for the half circular electric field with potential drop due to the electrode polarization. The maximum electrophoretic displacement can be determined based on the amplitude of the oscillatory motion as

$$X_{EP} = \frac{\varepsilon\varepsilon_0\zeta_p}{\eta}\left(\frac{\beta V_0}{\pi r}\right) G\left(\frac{\omega a^2}{\nu}\right)\frac{2}{\omega}. \tag{2.11}$$

2.3.5 Brownian Motion

With the use of the Stokes-Einstein relation ($D=k_BT/6\pi a\eta$), the expressions for characteristic displacements induced by random Brownian motion in one dimension is given by[40]

$$X_{Brownian} = \left(\frac{k_B T}{3\pi a \eta} t \right)^{1/2}, \tag{2.12}$$

where k_B is the Boltzmann constant and T is the temperature.

From the expression of each transport mechanism, comparisons of maximum displacements were obtained for scaling analysis. Figure 2.3 shows the result of scaling analysis using 30 μm electrode spacing, 1 μm polystyrene particle properties, which are ε_p=2.55, ρ_p=1050 kg/m^3, and σ_p=0.01 S/m.[49] The homogeneous particle model was used with the parameters, ε=78.5, D=1×10^{-9} m^2/s, ρ=1000 kg/m^3, μ=1×10^{-3} Ns/m^2, V=10 V. Relative magnitudes of characteristic particle displacement for each transport mechanism were compared, and the dominant transport mechanism with the largest displacement magnitude was predicted, as shown Figure 2.3a. At conductivities less than 10^{-4} S/m (i.e., typical range of DI water), electrode polarization effects induce dominant

AC-EO motion of the fluid at low frequencies (1~10 kHz). However, positive DEP starts to dominate as frequency increases, and negative DEP becomes significant after the crossover frequency (about 2 MHz). At conductivity values more than 10^{-2} S/m, positive DEP disappears because polarizability of the particle is less than that of the medium and the CM factor is negative over the whole frequency range. The AC-EO and negative DEP motions are relatively small at low frequencies where only Brownian motion is dominant. As frequency increases, AC-EO and negative DEP become dominant consecutively. Figure 2.3b shows the magnitude of the particle displacement in log scale normalized by its maximum value to represent the difference in an order of magnitude. As seen on the results, EP displacement is not dominant for the whole range

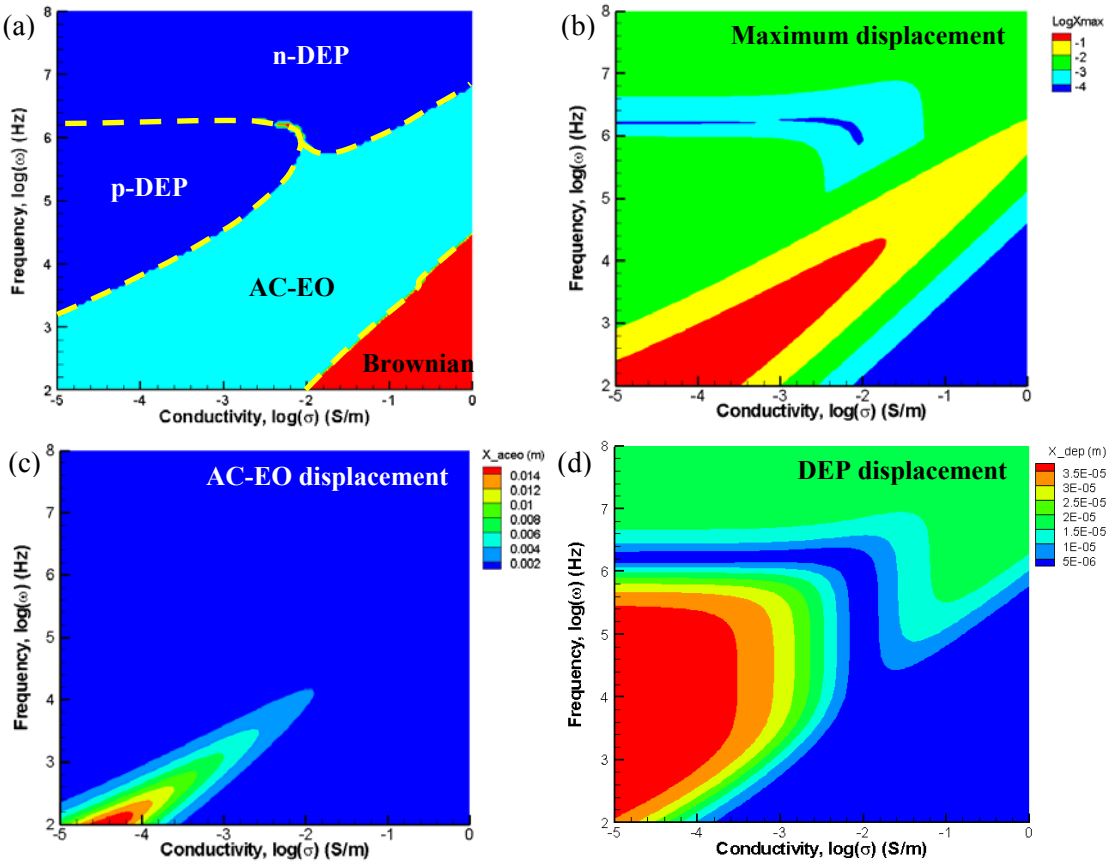

Figure 2.3 (a) Frequency-conductivity phase diagram for polystyrene particles. (b) Predictions of normalized particle displacement in a second as a function of the frequency and conductivity (normalized by the maximum, 1.62×10^{-2} m). Particle displacement due to AC-EO (c) and DEP (d). Homogeneous particle model was used with the parameters, ε_p=2.5, σ_p=0.01 S/m, ρ_p=1050 kg/m^3, ε=78, D=1×10^{-9} m^2/s, ρ=1000 kg/m^3, μ=1×10^{-3} Ns/m^2, V=10 V, a=0.5 μm and r=15 μm.

of interest. The maximum particle displacement occurs for AC-EO, and the Brownian motion is four orders of magnitudes smaller than the AC-EO motion. The dimensional values of AC-EO and DEP displacements are plotted in parts c and d of Figures 2.3. These two motions are limited by the electrode polarization effect, which is a function of the nondimensional frequency Ω. From eqs 3 and 7, it can be seen that displacements of AC-EO and DEP go to zero as Ω approaches zero. Thus, both transport mechanisms become insignificant in the low frequency and high conductivity region, and Brownian motion dominates.

It should be noted that the scaling map is generated to determine the dominant transport mechanisms based on the two-dimensional electric field assumption. Thus, spatial variations for each transport mechanism, especially in three-dimensional cases, cannot be accounted for precisely. However, these results are still applicable in design of more complex electrode systems because the complicated geometry of the electrodes can be divided into several sub regions with different characteristic lengths, allowing predictions of local colloidal motion.

It also should be noted that electrokinetic manipulation of particles is not possible in some regions of the scaling maps due to electrolysis effects. We experimentally observed electrolysis at frequencies below 800 Hz and voltages above 1 V. To avoid electrode damage, experimental validations of the scaling maps described in the next section were conducted outside the electrolysis range. We also observed that electrothermal effects were insignificant in the ranges of experiments (~10 V). However, electrothermal effects can possibly dominate colloidal motion at higher voltage inputs,

especially for cases with high conductivity buffers, because the power dissipation is directly proportional to the conductivity ($W \sim \sigma E^2$).[31] Although theoretical expressions are available, electrothermal effects are essentially related with three-dimensional flow motions and a different characteristic length scale is required to include electrothermal motions to the scaling analysis.[40] Thus, explicit comparisons with other AC electrokinetic forces are not attempted in this section. Effects of electrothermal motions are discussed in detain in Section 4.

2.3.6 Experimental Validations

The theoretical results are validated through experimental observations of particle motion utilizing interdigitated microelectrodes with 30 μm spacing. Three different types of particles, 1 μm polystyrene particles (polymer), 800 nm gold particles (metal), and *C. sporogenes* bacterial spores (biological species), were tested for examining the effect of polarizability of each particle. Randomly dispersed particles in the initial state were started with, and a steady-state distribution of the particles was observed in each case after applying electric fields. The dominant transport mechanism was determined based on the particle distribution and was compared with the scaling analysis. Properties of the particles and ionic solutions that were used in the scaling analysis are summarized in Table 2.1. Figure 2.4 shows the results of scaling analysis for 1 μm polystyrene particles with experimental observations of particle motion suspended in distilled water, which has a conductivity of 2.6×10^{-3} S/m. A random distribution of particles inside the fluid chamber was established in the initial state by feeding a fresh particle solution for each case. After application of a 10 V peak-to-peak

Table 2.1 Properties of colloidal particles and ionic solutions used in the scaling analysis

particle	polystyrene	gold	*C. sporogenes*
diameter	1 μm	800 nm	1 μm
conductivity (σ_p)	10^{-2} S/m	4.9×10^{7} S/m	10^{-2} S/m
buffer solution	**distilled water**	**NaHCO3 (0.1 mM)**	**DI water NaCl (0.1 and 1 mM)**
conductivity (σ)	2.6×10^{-3} S/m	1.8×10^{-3} S/m	1.0×10^{-5} S/m 1.3×10^{-3} S/m 1.3×10^{-2} S/m
diffusivity (D)		10^{-9} m^2/s	
viscosity (η)		10^{-3} Ns/m^2	

AC electric field for 5 min at specified frequencies, the steady-state distribution of the particles was captured. Each test case is indicated on the phase diagram and the particle displacement map, as shown in parts a and b of Figures 2.4. Scaling maps are plotted in a frequency-conductivity plane to demonstrate the transition of the dominant transport mechanism as a function of these two parameters. Effects of other parameters can be explained on scaling maps in different planes. We also observed the voltage dependence of the dominant transport mechanism utilizing a voltage-frequency phase diagram for the same buffer conductivity and found that the transition is dependent only on the applied frequency, with the exception of low voltage regions (less than 1 V) where Brownian motion was mostly dominant. As predicted from the scaling analysis, transition of the dominant transport mechanism can be seen on the experimental results, presented in Figure 2.4c. Alternating current electroosmotic motion was observed at the 1 kHz (case

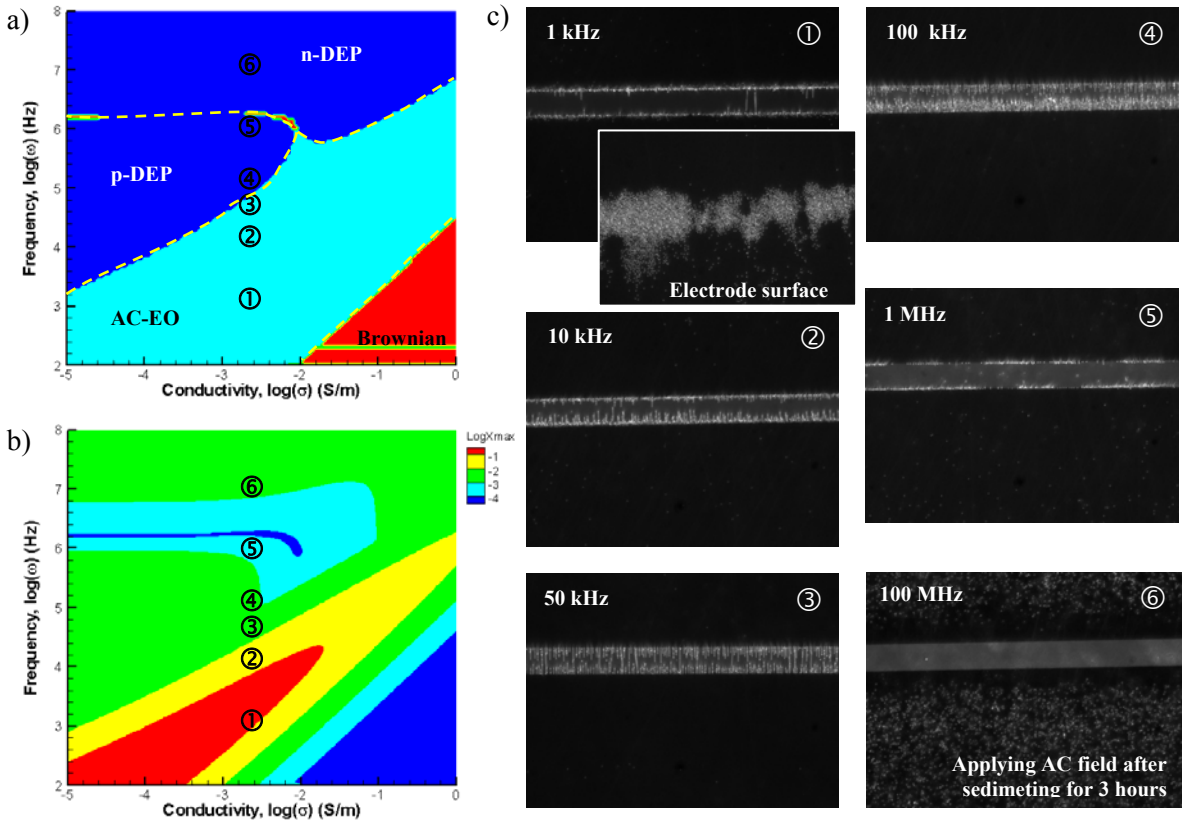

Figure 2.4 (a) Frequency-conductivity phase diagram for 1 μm polystyrene particles. (b) Normalized particle displacement as a function of frequency and conductivity with loci of six experimental results (normalized by the maximum displacement of 1.62×10^{-2} m). (c) Steady-state distribution of 1 μm polystyrene particles suspended in distilled water (2.6×10^{-3} S/m) after applying a 10 V peak-to-peak AC electric field for 5 min at specified frequencies. For image ①, concentrated particles on the center of the electrode surface driven by the AC-EO mechanism are also shown. Because of the nature of negative DEP that repels particles away from the electrode surface, the particles for case ⑥ were sedimented for 3 h to capture the lateral motion of particles at the image focal plane.

①), where a large amount of particles were concentrated on the center of the electrode surface, as predicted by the scaling analysis in Figure 2.4a. With increased frequency, the particles were forced to move toward the electrode gap and concentrated on the edges of the electrodes by positive DEP motion. The strength of positive DEP was increased as the frequency was gradually increased up to 100 kHz (cases ②, ③, and ④). However, the DEP motion was decreased at 1 MHz (case ⑤). The increase in positive DEP till 100 kHz frequency can be explained with a decrease of AC-EO motion, which competes with the positive DEP force. As seen in Figure 2.3c, AC-EO motion decreases as the frequency increases over 10 kHz at a conductivity of 2.6×10^{-3} S/m. Because the positive DEP and AC-EO are effective in opposite directions, positive DEP increases as AC-EO decreases. In case ②, small amounts of particles were observed on the center of the electrode surface, whereas positive DEP motion was dominant on the electrode gap. This can be interpreted as a result of competition between the AC-EO motion of the bulk fluid and the positive DEP, where AC-EO motion is affecting the particle transport far from the electrode edges at 10 kHz frequency. Although the scaling map predicts the AC-EO dominant transport of particles at 10 kHz frequency, positive DEP is effective near the electrode gap. In order to obtain more precise theoretical predictions near the region where AC-EO and DEP are balanced, further correlations with the experimental results for AC-EO motion by deriving an empirical value of capacitance ratio, Λ, in eq 2.1 would be required. Decrease of positive DEP near the crossover frequency (about 2 MHz) and negative DEP motion of particles at 10 MHz are well captured by cases ⑤ and ⑥. Because of the nature of negative DEP that repels particles away from the

electrode surface, particles for case ⑥ were sedimented for 3 h prior to the experiments, which enabled observation of lateral motions at the focal plane of the image.

Figure 2.5 shows theoretical and experimental results for 800 nm gold particles suspended in 0.1 mM $NaHCO_3$ buffer solution. Images were captured after applying an electric field at a specified frequency and voltage for 15 s. Figure 2.5a,b shows a theoretically predicted dominant force map in the frequency-voltage phase plane at buffer conductivity of 1.8×10^{-3} S/m and normalized maximum displacement of particles in the log scale. As shown in the figure, only AC-EO and positive DEP appear as dominant transport mechanisms except in the low voltage region where Brownian motion is dominant. Unlike the polymeric particles, polarizability variation of gold particles is negligible due to its higher conductivity (4.9×10^{7} S/m) compared to that of the buffer solution. Therefore, only a positive DEP force appears over 50 kHz. Figure 2.5c shows experimental results consistent with the scaling map. At 1 kHz frequency (cases ①, ④, and ⑦), the particles were driven to the center of the electrode by AC-EO motion. The strength of the AC-EO motion was increased with increased voltage, and more particles were concentrated on the center of the electrode. For frequencies higher than 1 kHz, particles were concentrated on the edges of the electrodes due to positive DEP motion. For cases ② and ③, weak positive DEP motion was observed near the electrode gap, while Brownian motion was observed away from the electrodes as predicted in the phase diagram. With increased voltage, more particles were concentrated and pearl chains of particles were formed between the electrodes. Figure 2.6 shows results of continued experiments using 800 nm gold particles under higher

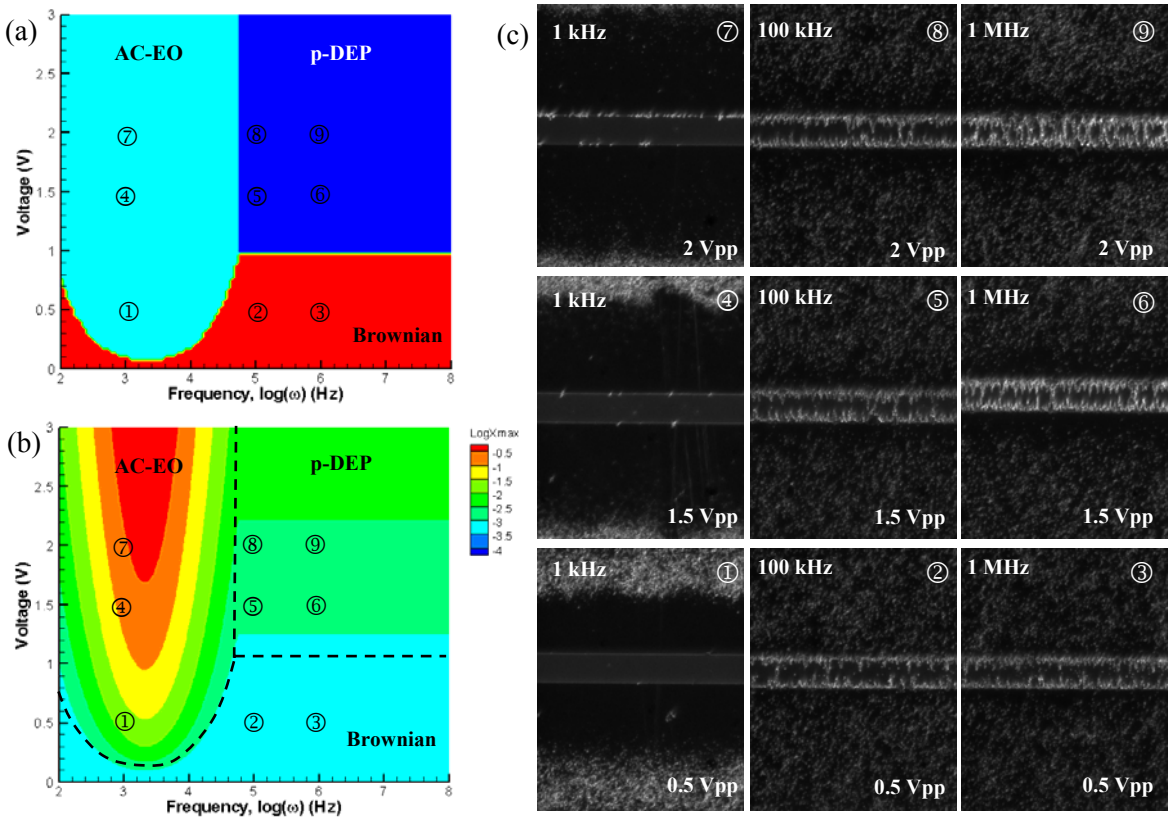

Figure 2.5 (a) Voltage-frequency phase diagram for the 800 nm gold particles. (b) Normalized particle displacement as a function of voltage and frequency with loci of nine experimental results (normalized by the maximum displacement of 1.72×10^{-3} m). (c) Steady-state distribution of 800 nm gold particles suspended in 0.1 mM $NaHCO_3$ buffer solution (1.8×10^{-3} S/m) after applying the specified AC electric field for 15 s.

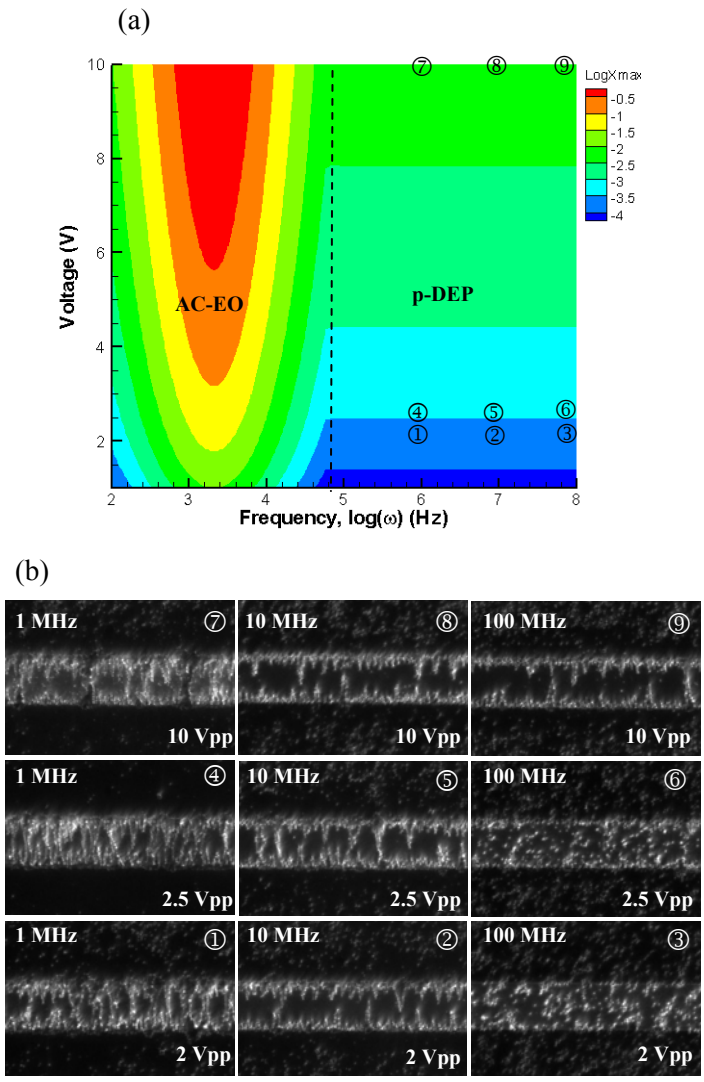

Figure 2.6 (a) Normalized particle displacement for 800 nm gold particles as a function of voltage and frequency with loci of nine experimental results (normalized by the maximum displacement of 1.90×10^{-2} m). (b) Steady-state distribution of 800 nm gold particles suspended in 0.1 mM $NaHCO_3$ buffer solution (1.8×10^{-3} S/m) after applying the specified AC electric field for 15 s.

frequencies and voltages. Positive DEP progressively disappears as frequency reached 100 MHz, and only weak positive DEP motion was observed for the 10 V voltage (case ⑨), whereas the scaling map does not predict the decrease of positive DEP at the high-frequency range. It can be conjectured that such high-frequency electric fields do not provide enough time for relaxation of the induced dipole moment on gold particles, and thus overall effective dipole is reduced due to dielectric loss. The characteristic relaxation time of polarization is dependent on the chemical composition and structure of the materials, and the temperature.[50] Thus, in order to predict the decrease of positive DEP by considering dielectric loss at high frequencies, more detailed models of complex electric permittivities of the particle and buffer solution would be required.

Figure 2.7 shows theoretical and experimental results for *C. sporogenes* bacterial spores suspended in ionic solutions with various conductivities. Conductivity of the suspending medium was varied by adjusting the molarity of the NaCl solution, and images were captured after applying a 10 V electric field at various frequencies for 1 min. In the case of biological species, an effective description of particle polarizability is required due to the variations in particle size and shape, and complex inner structure of the species. For non-homogeneous particles, the layered shell model can be used to describe the particle polarizability simply by using uniform dielectric properties for each layer.[46] However, it is usually difficult to develop a detailed model, which includes the effects of size and shape variations, and species specific dielectric parameters for bacterial spores. In order to reduce the time for detailed modeling, we approximated bacterial spores to have a spherical shape with a 1 μm average diameter and used a

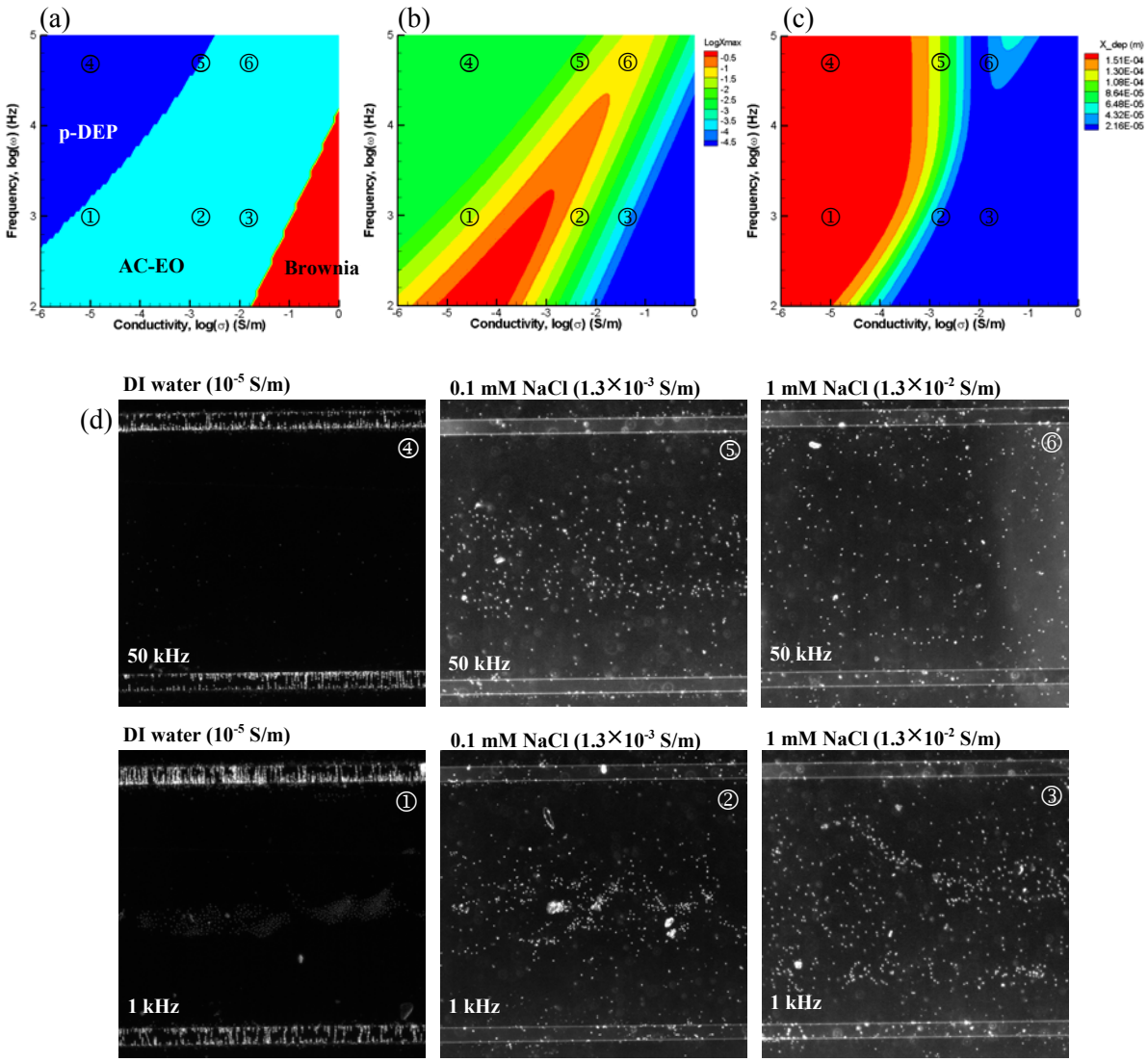

Figure 2.7 (a) Frequency-conductivity phase diagram for *C. sporogenes* spores. Particle displacement normalized by the maximum displacement of 1.62×10^{-2} m (b), and dielectrophoretic displacement (c) as a function of frequency and conductivity with loci of six experimental results. (d) Steady-state distribution of *C. sporogenes* spores suspended in buffer solutions with various conductivities after applying AC electric fields at specified electric field frequencies for 1 min. The ionic strength of the buffer solution was varied by adjusting the molarity of the NaCl solution.

simple solid model for describing the spore's behavior based on experimental observations. *C. sporogenes* spores have shown scalable motion with the frequency and amplitude of the electric field, without a second crossover in the DEP spectra within the 1 kHz to 100 MHz frequency range. This initial observation of DEP characteristics allowed simple correlation of scaling analysis for spores with the experiments based on a crossover frequency measurement.[49] Figure 2.7a,b shows the theoretically predicted dominant force and normalized maximum displacement in the frequency-conductivity phase plane. For the low conductivity solution (10^{-5} S/m), the theoretical result shows a decrease of AC-EO strength and transition to dominant positive DEP motion near the 1 kHz frequency (case ①) and predicts positive DEP dominance at 50 kHz (case ④). Consistent experimental results are demonstrated in Figure 2.7d. In case ①, positive DEP and AC-EO motion of spores are captured at the electrode gap and on the electrode surface, respectively. This can be interpreted as the transition of the dominant force from AC-EO to positive DEP. For the result with 0.1 mM NaCl buffer solution, dominant AC-EO motion is observed at 1 kHz (case ②), and the strength of AC-EO is decreased at 50 kHz (case ⑤). The transition to dominant positive DEP motion is predicted for case ⑤ in the phase diagram. However, positive DEP motion of the spores on the electrode gaps, such as in case ①, is not observed, because the strength of positive DEP is decreased as the conductivity is increased, as shown in Figure 2.7c. In the case of the 1 mM NaCl buffer solution, case ③ shows decrease of spore concentration on the electrode surface, and the strength of AC-EO motion is decreased compared with 0.1 mM case (case ②) as predicted in the scaling map. At 50 kHz (case ⑥), it can be seen on the image that AC-

EO motion is considerably reduced and only a few spores are driven away from the electrode edges. This decrease of AC-EO strength in case ⑥ deviates from the theoretical result, which predicts increased AC-EO motion compared with case ⑤. In order to obtain accurate theoretical results for AC-EO motion, capacitance parameters (C_S, C_D) should be correlated with the actual response of the double layer. We plan further studies to determine capacitance values of the double layer by analyzing impedance characteristics of the system, especially for high conductivity buffer cases where the capacitance of the diffuse layer is significant.

Experimental validation of the scaling map was continued for the spores suspended in DI water with various electric frequencies and voltages, as shown in Figure 2.8. Figure 2.8a shows the scaling map of normalized displacement with the frequency-voltage phase plane. It can be seen that AC-EO, positive DEP, and negative DEP progressively dominate the motion of the spores as frequency increases, whereas the overall magnitude of spore motion is increasing with the applied electric field. Experimental results, shown in Figure 2.8b, demonstrate strong positive DEP at 1 kHz (cases ① and ⑤), while positive DEP decreases as the frequency approaches to the crossover value (~2 MHz). At 10 MHz (cases ④ and ⑧), spore concentration cannot be observed at the focal plane due to the onset of negative DEP, which has been predicted by the scaling map. Thus, most of the spores were repelled from the electrode surface, and concentration of spores could not be achieved at the focal plane of observation.

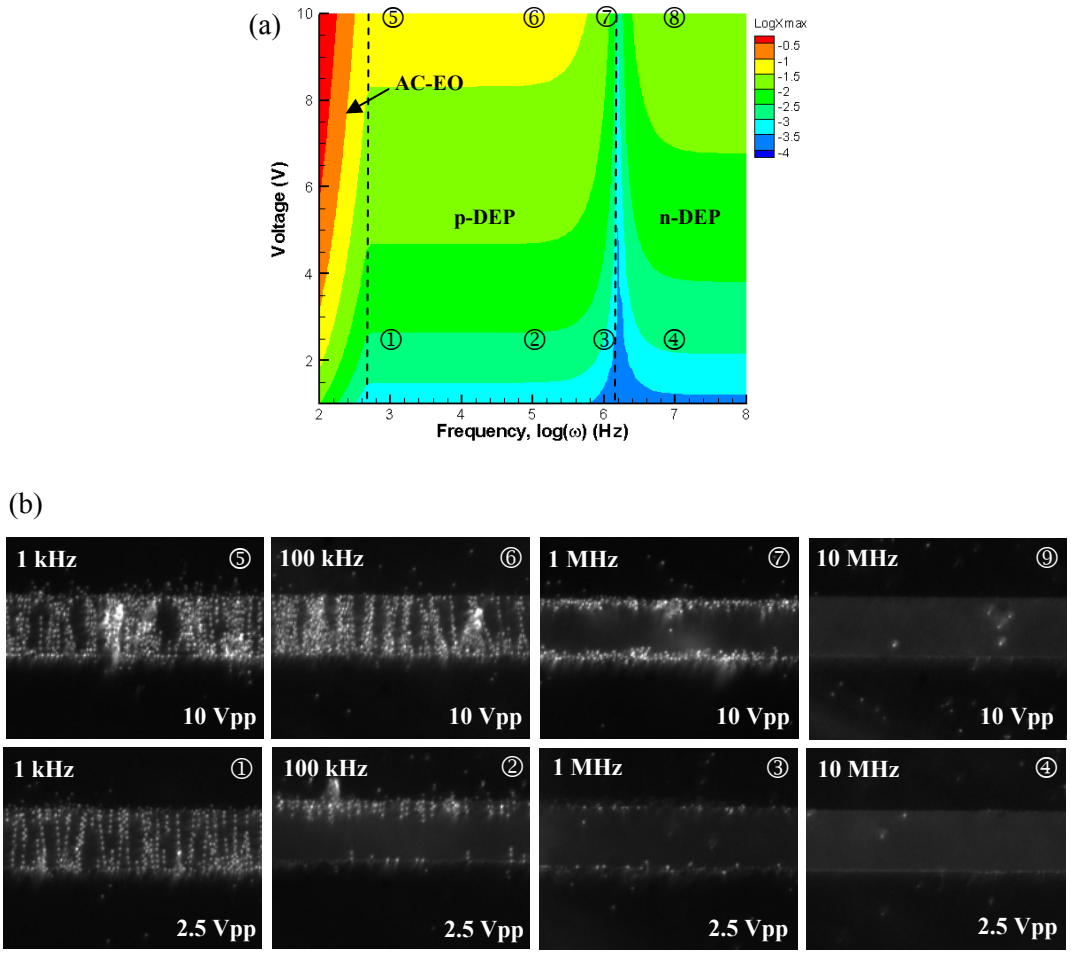

Figure 2.8 (a) Normalized particle displacement for *C. sporogenes* as a function of voltage and frequency with loci of eight experimental results (normalized by the maximum displacement of 3.30×10^{-2} m). (b) Steady-state distribution of *C. sporogenes* spores suspended in DI water (10^{-5} S/m) after applying the specified AC electric field for 1 min.

2.4 Conclusions

A theoretical predictive tool for AC electrokinetic manipulation of micrometer sized particles in a microfluidic device has been presented. With the utilization of a scaling analysis that considers relative magnitudes of EP, DEP, AC-EO, and Brownian motion, dominant transport mechanisms and their orders of magnitudes were explained over broad ranges of electric field frequency, amplitude, and ionic strength of the suspending medium. The resultant theoretical model was validated through parametric experimental examination of different types of colloidal particles including polymer (polystyrene), metal (gold), and biological species (*C. sporogenes* bacterial spores) with interdigitated electrodes. The AC electrokinetic motion of colloidal particles at various conditions of the electric field and suspending medium were well described in a predictive manner. Quantitative information of AC electrokinetic mechanisms for target species and media over a broad range of electric field frequency and amplitude enables configuration of the required electric field in the early design stages and provides an easy way to design frequency specific manipulations of various colloidal particles suspended in aqueous media without detailed numerical simulations. Therefore, the presented model can be applied in the design and optimization of future AC electrokinetic devices in an effective way.

3. DIELECTROPHORETIC TRAPPING OF BACTERIAL SPORES FROM HIGH CONDUCTIVITY MEDIA

3.1 Introduction

Rapid and reliable detection of pathogens is of great importance in food safety, water and environmental monitoring and clinical diagnosis.[51] Culture and colony counting method and polymerase chain reaction (PCR) are the most common tools used for pathogen detection so far. However, these methods generally require long processing time with well supervised operation, and are not free from costs of special equipments and labour inputs. As a promising solution for continuous and real-time detection, several biosensors are being developed recently. With a specific recognition probe such as an enzyme, nucleic acid, cell, antibody and molecularly imprinted polymer, biosensors can be utilized for the detection of pathogens with a number of methods including the optical, mass, electrochemical, and thermal techniques.[52, 53] Biosensor technologies involve trapping of particles onto detection surfaces of the sensor. Effectiveness of the surface-based detection can be limited by low concentration of particles, and selective trapping of target species on probe surfaces becomes important to improve detection limit of biosensors. Trapping of target species can be done in a passive manner with diffusion dominated transport, however, it occurs over relatively long time scale (order of hours). Thus, active manipulation techniques are required to achieve much shorter analysis time (order of minutes) and lower detection limit.[53]

Active manipulation of colloidal particles can be induced through the application of a variety of physical forces, including mechanical, fluidic, optical, acoustic, electrokinetic and electromagnetic.[36] Among these forces, dielectrophoresis (DEP) has several advantages such as remote manipulation of particles by electric field control and simple configuration of devices without mechanical moving components.[54] The utilization of DEP is increasingly effective as device dimension decreases to microscale, and such small devices can be readily integrated/packaged with other conventional electronic components with simple and inexpensive fabrication methods. DEP is the motion of polarizable particles that are suspended in an ionic solution and subjected to a spatially non-uniform electric field. Since the dielectric force depends on polarizability of the particles, DEP can be used to separate specific species even among similarly sized and charged particles. When the induced dipole moment on the particles is larger than that of the fluid, the particles move towards regions of the high electric field density (positive DEP). If the fluid is more polarizable than the particles, the particles move away from the high electric field density (negative DEP). It is possible to induce frequency specific variations in particle polarizability using AC electric fields, which further enriches the realm of DEP applications.

Positive DEP has been utilized for trapping and separating colloidal particles by several researchers using interdigitated, grid, point-and-lid, and ring-dot electrode configurations.[55] Positive DEP is very effective to concentrate target species from low conductivity media such as water.[56, 57] However, the utilization of positive DEP

is restricted by the requirement of relatively low conductivity media. The magnitude of the positive DEP force quickly diminishes when the conductivity of the media is increased. Thus, capturing biological species from high conductivity media using positive DEP is severely limited. This issue is especially important for handling living microorganisms, since using low conductivity buffers often result in high mortality rate of microorganisms due to an excessive osmotic stress.[32]

An alternative approach for trapping targets from a high conductivity medium is utilizing negative DEP, which repels particles towards the local electric field minima. Several electrode designs that amplify the negative DEP are castellated, quadrupole, and micro well electrodes based on two dimensional geometries, and octopole, insulator based DEP, and CMOS chip system with three dimensional configurations.[55] For sample manipulation using negative DEP, the electrodes should be designed to trap the targets efficiently in a selective capturing area, and fabrication of the device should be simple and inexpensive. The quadrupole electrode can be designed by a simple mathematical approach to create a single minimum electric potential well.[58] However, it requires four electrodes with opposite phases, and thus the repetition of electrode pattern to create multiple trapping zones is limited. The micro well electrode was mainly developed for single cell positioning inside a square electrode, and efficient trapping of single cell was demonstrated using a relatively simple geometry.[59] However, it had non-symmetric configuration that allowed secondary low electric field zones. The other three dimensional electrode systems could create well defined electric field minima[60] whereas they require

complicated fabrication process, including electrode deposition on both the top and bottom surfaces of the channels with spatial alignment of electrodes. Moreover, the particles were trapped inside the microchannel, not on the bottom or top side of the device, making it difficult for capturing the targets. Another important issue that should be considered for efficient negative DEP trapping is the electrothermal effect in high conductivity media.[31] Power dissipation from the electrodes causes temperature variation inside the suspending media. As a result, convective fluid motion can be induced. Conductivity of the suspending media is directly linked with the amount of dissipated power. Thus, the electrothermal motion of the fluid and the resultant viscous drag force exerted on a particle become significant as the media conductivity increases. In order to induce dominant DEP motion, the device scale should be reduced to amplify the DEP, while keeping the electrothermal effect due to power dissipation unchanged. Decreasing dimensions of the device reduces the sample capture area, lowering the device capacity. Therefore, trapping of target species from high conductivity media requires effective negative DEP traps with large capture area for useful operations.

Capturing yeast cells from 3.6×10^{-4} S/m and 0.015 S/m mannitol were successfully demonstrated using quadrupole and castellated electrodes, respectively.[58, 61] Four different kinds of bacteria were separated from a 0.01 S/m KCl solution using insulator based DEP.[57] Diluted phosphate buffered saline (PBS) with conductivity of 0.01 S/m and 0.002 S/m were used for capturing polystyrene beads on microwell and octopole electrodes, respectively.[59, 60] Patterning of yeast and

polystyrene beads on ITO electrodes were demonstrated inside 1.7×10^{-3} S/m diluted PBS and DI water, respectively.[61-64] Recently, capture of viruses suspended in 0.88 S/m physiological buffer using a quadrupole electrode was demonstrated.[65] However, this configuration requires four electrodes with opposite phases, and thus the repetition of electrode pattern to create multiple detection sites is difficult. Despite the urgent need for bio-particle manipulation for biomedical, environmental monitoring and food-safety applications, direct DEP trapping and patterning of biological species from high conductivity buffers (0.2 to 2 S/m) onto designated detection surfaces is limited.[66, 67] Hence, a simple and efficient DEP device that can manipulate biological samples within practical ranges of buffer conductivities is desired.

In this section, we present the design and development of a negative DEP based microfluidic device for trapping bacterial spores from apple juice (0.22 S/m) and milk (0.52 S/m) onto patterned surfaces where target specific probes can be implemented. These food sample matrices have four orders of magnitudes larger ionic concentrations than that typical deionized (DI) water. The specific objectives are:

- Theoretical prediction of DEP effectiveness in high conductivity media, such as food sample matrices and physiological buffers,
- Design of planar electrode for negative DEP trapping that allows easy fabrication and strong trapping onto patterned surfaces in high conductivity media (over 0.2 S/m),

- Experimental validation of negative DEP trapping of bacterial spores in complex food matrices.

3.2 Experimental Section

3.2.1 Microchannel Fabrication

Planar gold electrodes with different designs were deposited on pre-cleaned microscope slides (Gold Seal micro slide, Gold Seal) using conventional photolithographic techniques. Castellated and square block electrodes with characteristic length of 50 μm and 20 μm, respectively, were designed for negative DEP experiments. First, the microscope slide was cleaned in KOH solution for 15 minutes and immersed in acetone for 15 minutes. Slide was then rinsed with DI water (Simplicity, Millipore) and desiccated on a hot plate at 120 °C for 10 minutes. Positive photoresist (SC 1805, MicroChem) was spin-coated on the surface of slide to 1 μm thickness at 2000 rpm for 30 seconds. Soft baking was applied on a hot plate with ramped temperature variations, which were at 70 °C, 120 °C, and 70°C for 2 minutes each. The photoresist layer was exposed to ultraviolet light with mask aligner for 3 seconds and was left in air at room temperature for relaxation. The substrate was then developed in MF319 developer for 1 min and it was placed in reactive ion etcher (CS-1701, March Plasma Systems) for 10 seconds to remove any residues. After patterning the photoresist layer, a 5 nm-thick chromium layer and a 25 nm-thick gold layer were subsequently deposited on the substrate using metal

evaporation chamber (BOC 306, Edwards). By applying lift-off process in acetone, electrodes were obtained on microscope slide, as shown in Figure 3.1a. After attaching wires to the electrode ends, a cylindrical fluid chamber (10 mm diameter) was constructed by placing a 1 mm thick o-ring spacer on the observation area and was covered with microscope cover glass during the experiments, as shown in Figure 3.1b.

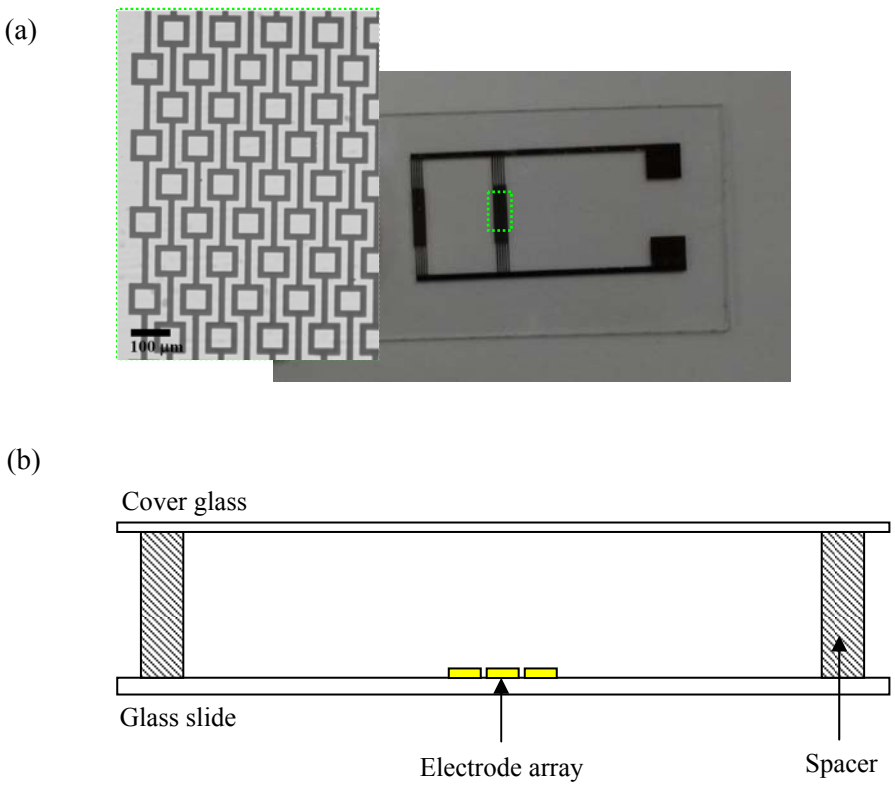

Figure 3.1 (a) Photograph of the gold electrode deposited on a microscope glass slide. (b) Schematic of microfluidic chamber configuration.

3.2.2 Experimental Conditions

Given the restrictions of using bio-threat agents for laboratory experimentation, we examined pathogen sample concentration utilizing *C. sporogenes* as the surrogate of a bio-threat agent, namely *Clostridium botulinum*. The spore sample was prepared as described in Appendix section. Experimental test solutions were prepared by mixing the stained *C. Sporogenes* spore samples with three different sample matrices – DI water, apple juice and 2% fat milk. The conductivity of milk and apple juice, measured with conductivity meter (PHH-80MS, Omega), were 0.2247 S/m and 0.5247 S/m, respectively. The resultant spore concentration was ~10^7 spores/ml. Test solution was then pippeted into fluid chamber, and 10 V peak-to-peak AC voltage was supplied by a function generator (AFG 3102, Tektronix) in a frequency range of 0~100MHz. Spore motion was observed with an optical microscope (TE2000-U, Nikon) and a 10X objective (0.3 NA). Images were captured using software (Insight, TSI) and CCD camera (PowerView1.4MP, TSI) with 1376×1040 pixel resolution (6.45 μm pixel size).

3.3 Results and Discussion

3.3.1 DEP Effectiveness

In case of an electric field with constant phase, time-averaged DEP force can be represented as[47]

$$F_{DEP} = 2\pi\varepsilon_0\varepsilon a^3 \,\mathrm{Re}\{K\}\nabla\left|E\right|^2, \tag{3.1}$$

where ε_0 and ε are the absolute permittivity and relative permittivity of the medium respectively, a is the particle radius, E is the electric field, and K is the Clausius-Mossotti (CM) factor. For a given particle and a suspending medium, DEP force is a function of the real part of CM factor, $\mathrm{Re}\{K\}$, and the magnitude of the electric field. The CM factor represents the effective polarizability of the particle with respect to the suspending medium, which is a strong function of the applied frequency. The $\mathrm{Re}\{K\}$ varies between +1 and −1/2. Positive DEP occurs for $\mathrm{Re}\{K\}>0$, which attracts the particles towards high electric field regions, *i.e.* electrode surfaces, while $\mathrm{Re}\{K\}<0$ causes negative DEP that repels the particles away from the electrodes. For non-homogeneous particles, e.g., biological cells, a layered shell model can be used to describe the particle polarizability by using uniform properties of each layer.[47] The layered shell model can be used to describe the particle properties more precisely, however, it is usually challenging to find out the required parameters for describing each layer. Thus, an effective method and appropriate parameters should be considered for modelling of target materials, especially for biological species with complex inner structure.

As described in Section 2, we used a solid model for describing the polarizability of the spores to reduce the time for detailed modelling. The resultant scaling map that considered relative magnitudes of particle displacements due to DEP, AC electroosmosis, electrophoresis and Brownian motion was correlated with

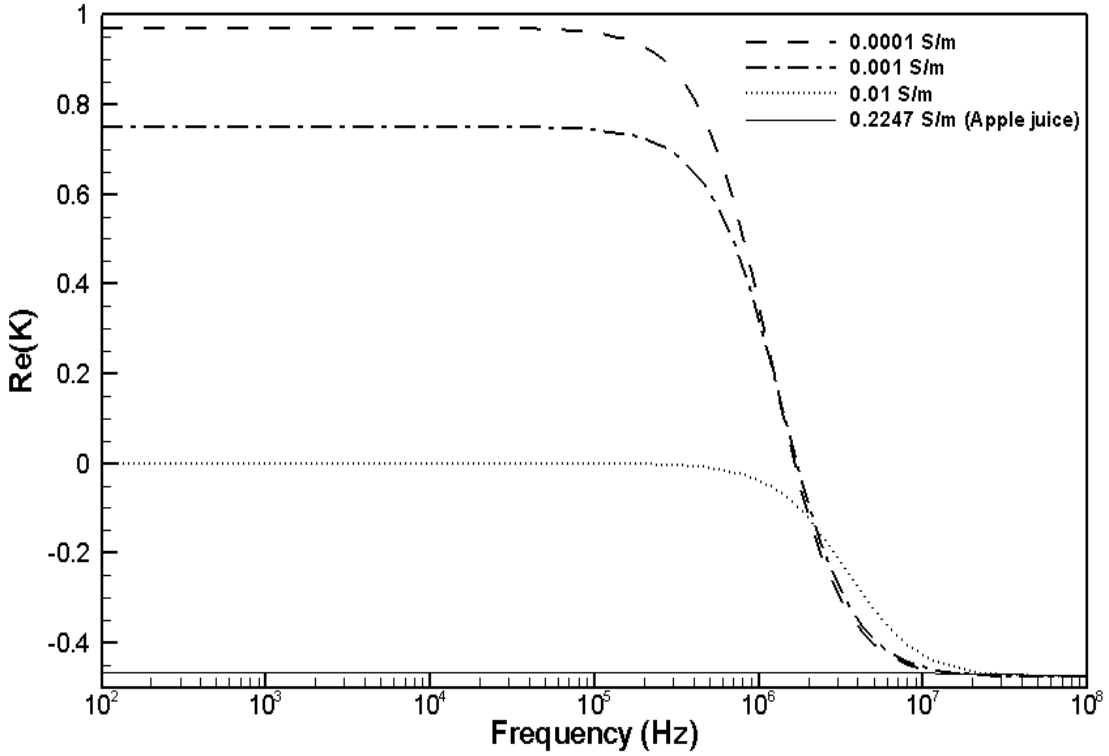

Figure 3.2 Plot of the real part of Clausius-Mossotti factor for a solid spherical dielectric particle at various medium conductivities. The physical parameters of bacterial spores, predicted by experiments, are ε_p=2.55, σ_p=0.01 S/m and ε=78.5.

experimental results obtained using planar interdigitated electrodes. For a homogeneous solid particle, the conductivity of the particle can be represented as $\sigma_p=\sigma_{p,bulk} + 2K_s/a$, where K_s is the surface conductance.[68] Figure 3.2 shows the frequency dependence of the CM factor utilized for the theoretical model. The real part of CM factor was calculated using equation 3.2 for four different media conductivities. The relative permittivity of the particle and medium were assumed as

2.55 and 78.5, respectively, and the conductivity of the particle was assumed 0.01 S/m. Effects of the conductivity of the medium on CM factor can be clearly seen in Figure 2. At conductivities lower than 0.01 S/m, particles experience positive DEP up to ~1 MHz, after which $\mathrm{Re}\{K\}<0$ and negative DEP is observed. Above 0.01 S/m, positive DEP cannot be used and negative DEP becomes effective at all frequencies. Interestingly $\mathrm{Re}\{K\}\sim 0$ up to 1 MHz at 0.01 S/m, and negative DEP becomes effective above this frequency. As can be observed from the figure, use of positive DEP for manipulation of spores suspended in apple juice and milk is restricted, since these food matrices have conductivities larger than 0.2 S/m.

In order to determine electric field frequency for the negative DEP trapping, the scaling analysis was conducted for the designed electrodes.[69] Figure 3.3 shows the phase diagram for variations of dominant forces and magnitude of the DEP transport. It can be seen that negative DEP motion is dominant with respect to other forces, AC electroosmosis and Brownian motion, only at certain frequency range (Figure 3.3a), and magnitude of the DEP motion is varying as a function of the frequency and medium conductivity for fixed voltage and characteristic length (Figure 3.3b). Based on the theoretical prediction of scaling maps, experimental frequency range was selected for negative DEP trapping.

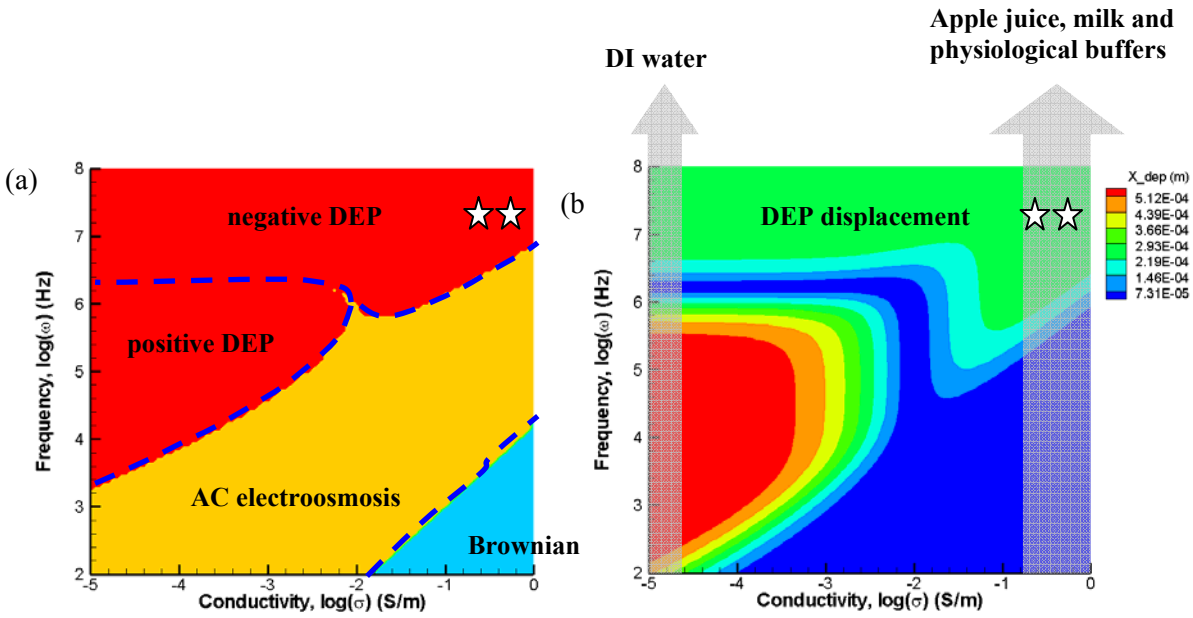

Figure 3.3 (a) Frequency-conductivity phase diagram. (b) Particle displacement (per second) due to the DEP force. Homogeneous particle model was used for the spores with the following parameters: ε_p=2.55, σ_p=0.01 S/m, ε=78.5, V=10 V_{pp}, a=0.5 μm and characteristic length r=10 μm. Frequency and conductivity values that correspond to the experimental conditions are specified on each plot with stars (50 MHz, 0.2247 S/m and 0.5247 S/m).

3.3.2 Negative DEP Trapping

Negative DEP drives particles towards lower electric field gradient zones. Because strong electric field exists on the electrode surface, the direction of negative DEP is usually outward from the electrode surface, which makes it difficult to capture

target species using conventional interdigitated electrode array (IDA). A well defined local minimum of electric field inside the microfluidic chamber is required to trap particles using negative DEP.

We designed and fabricated two different gold electrodes that can create low energy wells on the planar bottom surface. First electrode was the well-known castellated electrode with 50 μm separation. Pethig et al. successfully demonstrated manipulation of yeast cell suspended in 150 μS/cm mannitol solution with 80 μm spacing in castellated electrodes.[61] We repeated the experiment with smaller electrode spacing and bacterial spores were suspended in much higher conductivity media. Figure 3.4 shows the results of spore concentration on the bay area at two different electrode positions. Images of spores suspended in apple juice and 2% fat milk were taken after applying AC electric field at 10 V amplitude and 1 MHz frequency for 5 minutes. Upon application of the AC electric field, initially well dispersed spores were forced to move away from the high electric field zones (*i.e.* electrode tips), and they were continuously driven by convective motion of the bulk fluid. Although the spores experienced electrothermal effects, they gradually concentrated on the bay area between the electrode tips due to negative DEP. Once the spores were trapped inside the low electric field zones, trapping force was dominant enough to hold the spores against the fluid motion. Thus, the amount of captured spores was increased by time. Since the apple juice and milk have high electrical conductivities, shielding effect of the electric double layer is very weak, and most concentrated spores attached to the glass surface by van der Waals forces.

(a) Apple juice

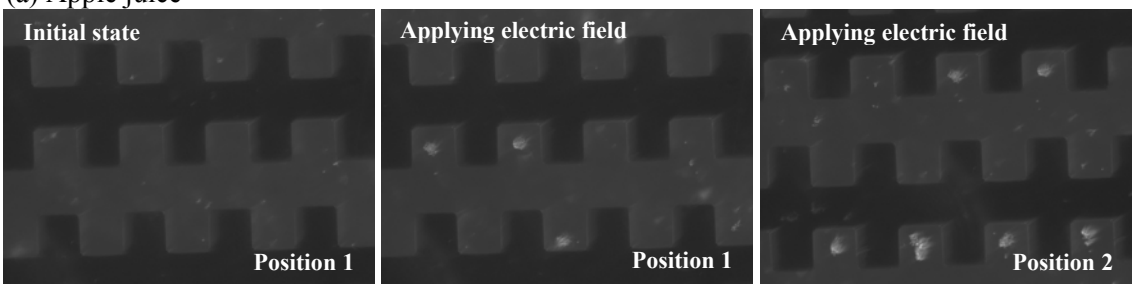

(b) 2% fat milk

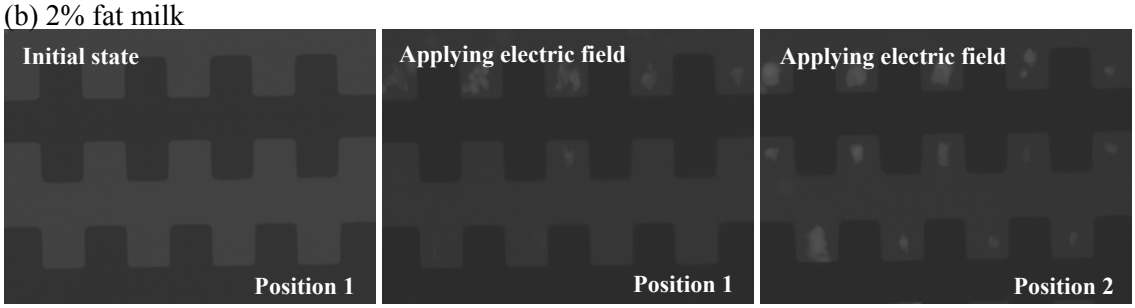

Figure 3.4 Images of *C. sporogenes* stained spores suspended in (a) apple juice and (b) 2% fat milk before (initial state) and after applying AC electric fields for 5 minutes at 10 V amplitude and 1 MHz frequency. Gold electrodes and glass are observed as dark and light gray, respectively, while the stained spores are white. Characteristic electrode separation is 50 μm.

The castellated electrodes have shown potential ability for trapping the spores using negative DEP. A saw tooth shape generates in-plane electric field variation and creates the low potential zone at bay area, isolated by the high electric field lines. However, increase of the effective bay area for enhancing local concentration of spores and improving detection limit is limited due to its successive configuration of

positive and negative patterns. Increase of the low electric field area causes longer separation distances between the interdigitated electrodes, which in turn results in decrease of the overall strength of the DEP trap. Moreover, design and optimization of electrodes may require detailed numerical results due to the complex electric field configuration including the three dimensionality effects. For local concentration and trapping of target species, effective electrode design is required for increasing the actual capturing area, and hence, scaling up the capacity of the unit device. Simple configurations of planar electrodes are desirable for the ease of electric field prediction and microfabrication.

In order to address the deficiencies of the castellated electrode geometry, we designed and fabricated simple planar square block electrodes that can create low energy wells on the planar bottom surface. The electrodes consist of interdigitated positive and negative electrodes with repeated patterns of square blocks. Separation between the electrodes was kept constant at 20 μm to reduce three dimensional variations of the electric field. Each interdigitated electrode has square patterns with 60 μm × 60 μm inner area, and a low potential well is created inside these patterns isolated by strong electric field between the positive and negative electrodes. This configuration made possible to trap colloidal particles only at designed areas inside the square blocks on a planar surface, which enables integration with diagnostic devices. For example, the square patterns can be exploited for probe surfaces of specific antibodies, and various kinds of biosensors such as optical, electrochemical, and piezoelectric biosensors[51] can be possibly integrated with the negative DEP trap

to identify target species. The effective area for negative DEP trap can be easily increased by repeating the patterns due to the symmetric design in both horizontal and lateral directions. Also, the low potential zones are created with relatively smaller net surface area of the electrodes, which in turn decreases heating from the electrodes.

Figure 3.5 shows spore capture from apple juice and milk at the designed negative DEP traps. Images were taken at two different electrode positions after applying AC electric field at 10 V amplitude and 50 MHz frequency for 5 minutes. With an initial random distribution inside the fluid chamber, spores interacted with hydrodynamic and DEP forces after applying the electric field. Spore concentration inside the square patterns increased gradually as the spores were continuously driven towards the electrode array by a convective motion inside the fluid chamber. A pair of convective rolls mainly delivered the spores to the electrode array at the middle part of the chamber, while the negative DEP force, dominant near the electrodes, trapped the spores inside square patterns. The trapped spores bounded on the glass surface due to the very thin electrical double layer in high conductivity media. This result demonstrates that the square block electrodes can successfully trap the spores at patterned surfaces in high conductivity media with geometric benefits of the planar and symmetric configuration.

(a) Apple juice

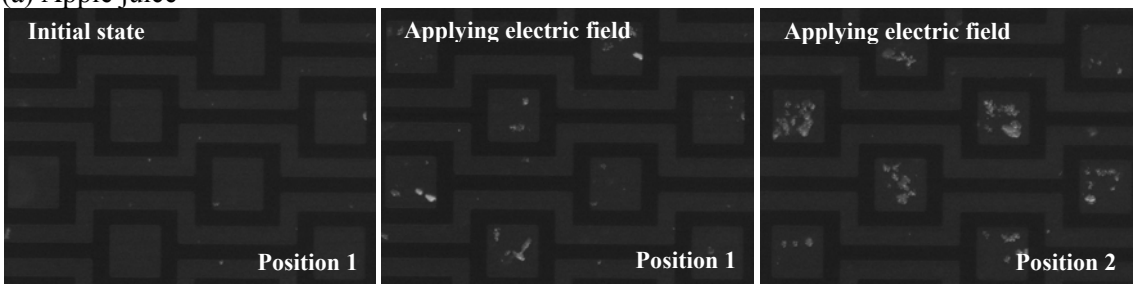

(b) Milk

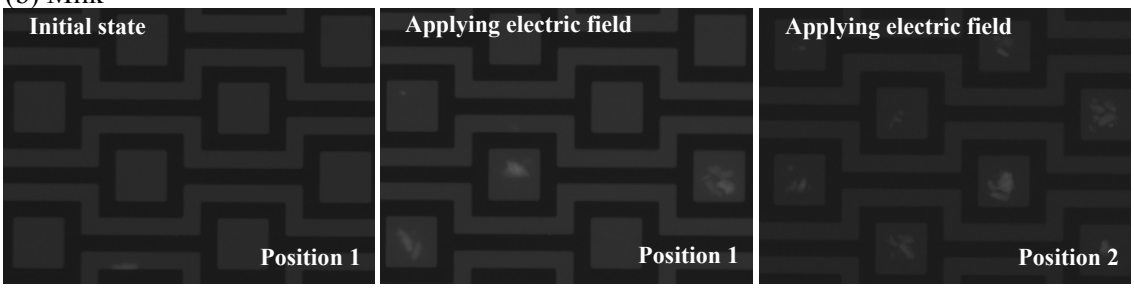

Figure 3.5 Images of *C. sporogenes* stained spores suspended in (a) apple juice and (b) milk before (initial state) and after applying AC electric fields for 5 minutes at 10 V amplitude and 50 MHz frequency. Gold electrodes and glass are observed as dark and light gray, respectively, while the stained spores are white. Characteristic electrode separation is 20 μm.

It should be noted that the presented device is also applicable for trapping of particles suspended in low ionic strength media. Figure 3.6 shows patterning results of 1 μm silica particles and 4 μm polystyrene particles suspended in 3.7 mM NaCl solution and DI water, respectively, after applying AC electric field at 10 V and 10 MHz for 30 seconds. Fast aggregation of particles on patterned surfaces was

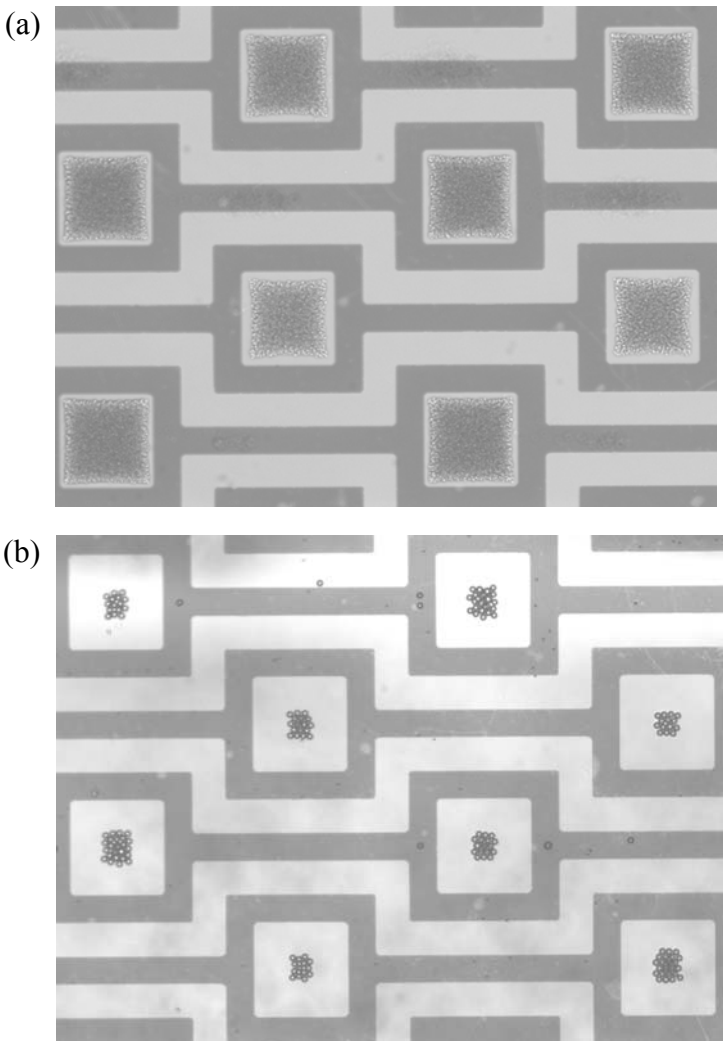

Figure 3.6 Images of trapped colloidal particles after applying AC electric field at 10 V amplitude and 10 MHz frequency. (a) 1 μm silica particles suspended in 3.7 mM NaCl solution (0.049 S/m). (b) 4 μm polystyrene particles suspended in DI water (1×10^{-5} S/m).

demonstrated in a low conductivity medium. Since high ionic strength of suspending media is not generally required in case of artificial particles, several researches focused on patterning of polystyrene beads using AC electric field in low conductivity media.[63, 64, 70, 71] Compared with the previously reported devices that utilize pair electrodes on the bottom and top surfaces of a chamber, the presented device shows fast patterning of particles with simple two dimensional configuration.

3.3.3 Effect of Fluid Motion

In the presence of AC electric fields, the electro-hydrodynamic (EHD) fluid motion can be induced by local temperature variations due to Joule heating or external heat sources.[72] The electric power dissipation in a medium by Joule heating effect is $W=\sigma E^2$, and thus the EHD motion of fluid becomes increasingly significant as the medium conductivity is increased. The local temperature variation results in the gradients of electrical properties and density of the suspending medium, which induces electrothermal flow and buoyancy-driven flow, respectively.[60] In our square block electrode experiment, a continuous convective fluid motion was observed inside the fluid chamber. The spores gradually accumulated at the middle part of the fluid chamber, suggesting dominance of the buoyancy-driven flow, while the negative DEP force was locally dominant near the electrodes to trap the spores inside patterned surfaces. The relative magnitude of the buoyancy force with respect to the electrothermal force can be estimated using the following relation [40]

$$\frac{f_{buoyancy}}{f_{electrothermal}} \sim \frac{(\partial\rho/\partial T)(\pi r)^3 g}{(1/\sigma)(\partial\sigma/\partial T)\varepsilon V^2}, \tag{3.2}$$

where g is the gravitational acceleration, ρ is density of the media, and T is the temperature. For a characteristic length scale r=1 mm (the chamber height in the experiment), this ratio is about 55, which in turn supports dominance of the buoyancy-driven flow in our observation. However, it has been reported that the buoyancy force becomes less dominant as a system characteristic length decreases, and a transition between buoyancy and electrothermal flow is expected to occur for a characteristic length around 300 μm.[40] Thus, the effect of electrothermal flow needs to be considered for the development of more compact systems. Electrothermal fluid motion and its effects on the DEP manipulation are further investigated in detail, and numeral and experimental results are presented in section 4.

3.4 Conclusions

A DEP based microfluidic device for trapping of pathogen samples from complex food matrices is presented. Negative DEP trap is utilized to capture *C. sporogenes* from high conductivity suspending media such as apple juice (0.2247 S/m) and milk (0.5247 S/m), which enables the direct use of buffer solutions within a practical range of conductivity. Effectiveness of DEP on bacterial spore capture is described using CM factor and scaling analysis. Planar electrodes with the square block design were fabricated to induce strong negative DEP traps. Specifically, the

square block electrode has well defined electric field minima that can act as the spore attachment/detection sites for integration of biosensors. In addition, the square block electrode can be scaled up to increase processing volume or to create multiple detection sites, by simply repeating the symmetric electrode patterns. Two-dimensional planar electrodes require simple chamber configuration and fabrication steps, which gives the square-block electrodes a competitive advantage over other existing negative DEP designs. Future studies include integration of the DEP capture unit with diagnostic devices and sample feeding components, enabling the development of a micro total analysis system for rapid detection of pathogens and other microorganisms in high conductivity food matrices.

4. ELECTROTHERMAL EFECTS ON DIELECTROPHORETIC COLLOIDAL MANIPULATIONS

4.1 Introduction

DEP based colloidal manipulations offer many advantages including remote and selective control of target species. DEP motion of particles can be induced in the presence of non-uniform electric field, which is typically generated by embedded electrodes inside a fluid chamber. Since application of AC electric field induces the polarization of particles as well as of suspending liquid, DEP motions of particles are usually affected by drag forces due to AC-EO motion of fluids polarized at electrodes' surfaces. In addition to the polarization effect of liquid media, particles also experience the Brownian motion and gravity. As discussed in section 2, electric fields of high intensities need to be generated to induce dominant DEP motion over other transport mechanisms by reducing the characteristic dimension of a device or increasing the magnitude of the applied voltage. However, such an amplified electric field causes local heating inside a fluid volume because of the increased energy dissipation in the system, and often the DEP force is overcome by the electrothermal motion of fluids. Electrothermal effect refers to the fluid motion due to the spatial variation of electrical properties of a liquid medium, induced by the temperature gradients due to the Joule heating in presence of AC electric fields. The effect of electrothermal motion becomes significant in the electrokinetic manipulation of high conductivity samples because Joule heating depends on the intensity of electric field,

as well as conductivity of the media. Thus, understanding the effects of electrothermal flow on DEP motion of particles is required for the development of physiological sample applications.

In section 3, we successfully developed a planar negative DEP trap for high conductivity media using the scaling analysis. The scaling analysis is a simple tool that provides the conditions for DEP dominance over the other electrokinetic forces based on the prediction of the relative magnitude of different electrokinetic displacements. However, electrothermal effects are not included in the scaling law because it is difficult to describe the three dimensional flow structure of the electrothermal motion in terms of a single characteristic length scale. Although the experimental observations have shown dominant DEP motions of target species on the designed electrode, a lack of characterization of electrothermal effects on DEP motion limits further modification of the device for amplifying the DEP strength and increasing the trapping efficiency.

In this section, we investigate the effect of electrothermal motion on DEP manipulations using numerical simulations and experimental observations. Our initial observations in the experiments of bacterial spores have shown that a buoyancy driven flow continuously provided the spores onto electrode array, and the amount of trapped spores was increased by time. In a similar way, we expect that electrothermal flow motions can be utilized to enhance DEP trapping by feeding particles onto trapping zones with the local circulatory fluid motion.[72, 74] The buoyancy force becomes negligible as a system characteristic length decreases, and the

electrothermal flow will induce symmetric local circulations around the trapping zones because our electrodes design is symmetric. The motivation of this study is to investigate the possible trapping enhancement on the designed electrode by using these circulatory motions of electrothermal flow. This work is organized as follows: in the next section, we introduce the physical background for electrothermal motion of fluids, and summarize the governing equations. In the following section, three dimensional numerical simulations for electric potential and flow fields are performed, and DEP force variation and electrothermal flow motion are described. Then, experimental observations of particle motion are conducted to compare with the numerical results. Finally, possible enhancement of DEP trapping due to electrothermal effects is discussed.

4.2 Theory

Temperature field due to Joule heating of electric fields can be determined by solving the energy equation, given as[73]

$$\rho c_p \left(\frac{\partial T}{\partial t} + u \cdot \nabla T \right) = \nabla \cdot (k \nabla T) + \sigma E^2 , \qquad (4.1)$$

where ρ is the fluid density, c_p is the specific heat, k is the thermal conductivity, and σ is the electrical conductivity. The last term in the equation, σE^2, represents the Joule heating. For sufficiently high frequencies, time dependent term can be omitted. For a typical microsystem, the heat convection, $\rho c_p u \cdot \nabla T$, is three orders of

magnitudes smaller than the heat diffusion, $\nabla \cdot (k\nabla T)$.[73] Neglecting the heat convection term, time averaged energy equation can be simplified as

$$\nabla \cdot (k\nabla T) + \left\langle \sigma E^2 \right\rangle = 0 . \tag{4.2}$$

The resultant temperature field produces gradients in the electrical permittivity, ε, and the conductivity, σ, of the liquid, which in turn results in charge density variation and electric field perturbation. The electrical force exerted on the fluid due to the variation of electrical properties can be represented as[73]

$$f_e = \rho_e E - \frac{1}{2}|E|^2 \nabla \varepsilon + \nabla\left(\frac{1}{2}\rho\left(\frac{\partial \varepsilon}{\partial \rho}\right)_T |E|^2\right), \tag{4.3}$$

where ρ_e is the charge density. The first and second terms are the Coulomb and dielectric forces, respectively. The last term is the electrostriction. Flow motion under the effect of the electrical body force is governed by the incompressible Navier-Stokes equation with a source term, given by

$$\rho\left(\frac{\partial u}{\partial t} + u(\nabla \cdot u)\right) = -\nabla p + \mu \nabla^2 u + \rho g + < f_e >, \tag{4.4}$$

where p is the pressure, g is the gravitational acceleration and μ is the viscosity. Using Boussinesq approximation and neglecting the convection term for low Reynolds number flow, the momentum equation can be simplified as[73]

$$-\nabla p + \mu \nabla^2 u + \Delta \rho g + < f_e >= 0 , \tag{4.5}$$

where the term $\Delta\rho g$ represents the buoyancy force. Incorporating the electrostriction term into the pressure term, time averaged electrical force can be written as[72]

$$< f_e >= \frac{1}{2}\mathrm{Re}\{\rho_e E^*\} - \frac{1}{4}E \cdot E^* \nabla\varepsilon, \tag{4.6}$$

where E and E^* represents the electric field and its complex conjugate, respectively. The charge density and the electric field are related with Gauss' law,

$$\rho_e = \nabla \cdot (\varepsilon E), \tag{4.7}$$

and the charge conservation equation,

$$\frac{\partial \rho_e}{\partial t} + \nabla \cdot (u\rho_e) + \nabla \cdot (\sigma E) = 0. \tag{4.8}$$

The second term can be neglected because the relative magnitude of the convection current, $\nabla \cdot (u\rho_e)$, compared to the conduction current, $\nabla \cdot (\sigma E)$, is small for typical microsystems.[73] The charge density induced by inhomogeneous electrical properties can be further simplified using a perturbation expansion in the case of small temperature variation. By expressing the electric field and the charge density in terms of constant average and perturbation terms, $E = \overline{E} + E'$ ($|E'| << |\overline{E}|$) and $\rho_e = \overline{\rho}_e + \rho_e'$ ($|\rho_e'| << |\overline{\rho}_e|$), respectively, equations 4.7 and 4.8 can be combined into the following single equation[72]

$$\rho_e' = \nabla\varepsilon'\cdot\overline{E} + \bar{\varepsilon}\nabla\cdot E' = \nabla\varepsilon'\cdot\overline{E} - \bar{\varepsilon}\frac{\overline{E}\cdot\nabla(\sigma'+i\omega\varepsilon')}{(\bar{\sigma}+i\omega\bar{\varepsilon})}. \quad (4.9)$$

Assuming the gradients of σ and ε due to the temperature increments are also small, we can express the variation of the electrical properties with perturbation terms in a similar way, and the equation 4.9 can be further simplified as[72]

$$\rho_e' = \frac{\bar{\varepsilon}(\alpha-\beta)}{1+j\omega(\bar{\varepsilon}/\bar{\sigma})}(\nabla T\cdot\overline{E}), \quad (4.10)$$

where $\alpha=(\partial\varepsilon/\partial T)/\varepsilon$ and $\beta=(\partial\sigma/\partial T)/\sigma$. Typical values for water, α=0.0046 K^{-1} and β=0.02 K^{-1}.[75] The resulting time averaged electrical force is expressed as[72, 73]

$$< f_e >= \frac{1}{2}\mathrm{Re}\left\{\frac{\bar{\varepsilon}(\alpha-\beta)}{1+j\omega(\bar{\varepsilon}/\bar{\sigma})}(\nabla T\cdot\overline{E})\overline{E}^*\right\} - \frac{\bar{\varepsilon}}{4}\alpha\overline{E}\cdot\overline{E}^*\nabla T. \quad (4.11)$$

In low frequency range, the first term on the right hand side (Coulomb force) is dominant while the second term (dielectric force) is dominant in high frequency range.

4.3 Numerical Simulation

A commercially available software, CFD-ACE, is used for the numerical simulation of electrothermal flow on the square block electrodes. Overall computational procedure can be summarized as follows: the electrical potential is computed by solving Laplace equation, $\nabla^2\phi = 0$, and the computed electric field, *E*, is used for the solutions of the energy and the momentum equations for the fluid, given by equations 4.2 and 4.5, respectively. DEP force field is also calculated using the resultant electric field and

equation 2.4. Figure 4.1 shows the computational domain and boundary conditions used in the numerical simulation. In order to reduce the computational cost, a quarter portion of the fluid volume on a single pattern of a square block electrode is modeled due to its symmetric shape. The simulation domain size is 80 μm × 120 μm × 1 mm. Insulating boundary conditions, $\partial T/\partial n=0$ and $\partial \phi/\partial n=0$, are used at the top and bottom surfaces with wall thicknesses of 150 μm and 1 mm, respectively, with the exception of the electrode surfaces, where constant temperature and electric potential are applied as ±5 V and 300 K. Symmetry boundary conditions are used for other faces.

Figure 4.2 shows the electric potential and temperature distribution near the electrode surfaces. As depicted in Figure 4.2a, the electric potential supplied from the bottom electrodes creates a non-uniform potential field inside the suspending medium. Variation of the potential field is negligible far from the electrodes, and the potential reaches a constant value above the height of 240 μm approximately. The resultant temperature rise due to the electric field is shown in Figure 4.2b. The temperature has the maximum value above the linear part of the electrode that interconnects each square shape, and it decays with reduced distance to the bottom surface. Since the temperature field is directly coupled with the electric field, a temperature gradient is generated only inside a small portion of the fluid volume near the bottom surface, and the temperature variation is negligible above a certain height. Induced temperature gradient influences the electrical properties of the liquid, which is a function of the temperature. The resulting electrothermal flow structure is shown in Figure 4.3. Flow distribution is plotted at two symmetric planes. Direction and

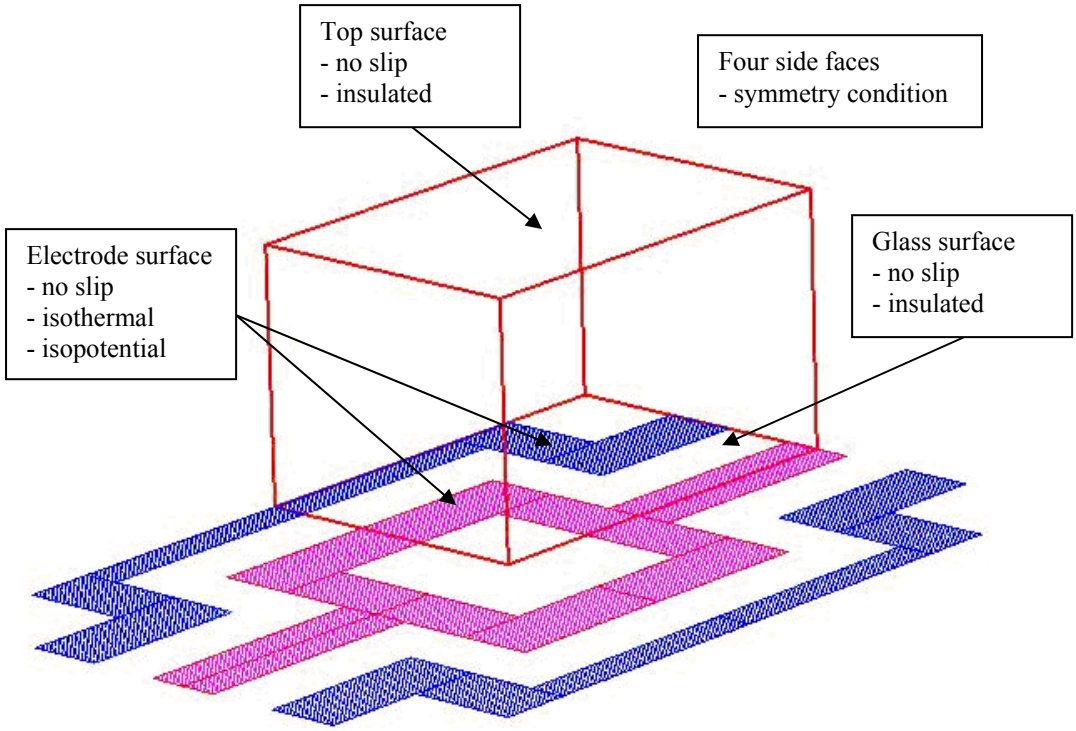

Figure 4.1 Simulation domain and boundary conditions for electrothermal flow. In order to reduce the computational cost, a part of the fluid volume on a square block electrode is modeled due to its symmetric shape. Simulation domain, shown as a cube with red lines, has 80 μm width, 120 μm length and 1 mm height. Insulating boundary conditions are used at the top and bottom surfaces with an exception of the electrode surfaces, where constant temperature and electric potential are applied. Symmetry boundary conditions are used for four side faces.

(a)

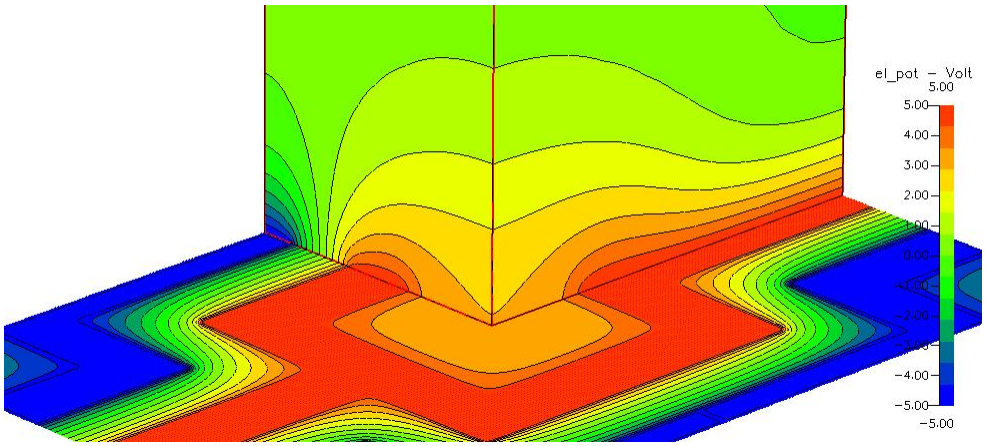

(b)

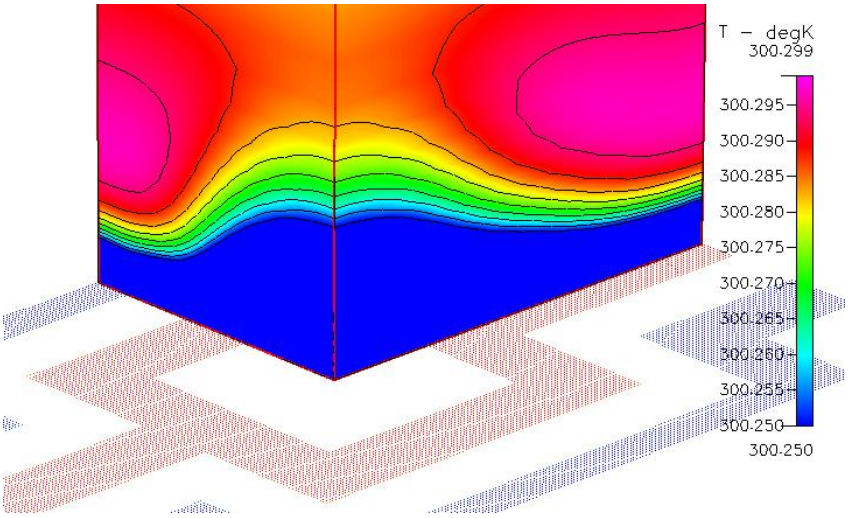

Figure 4.2 (a) Electric potential distribution near the electrode surface, and (b) temperature distribution at the symmetry planes at 10 MHz frequency.

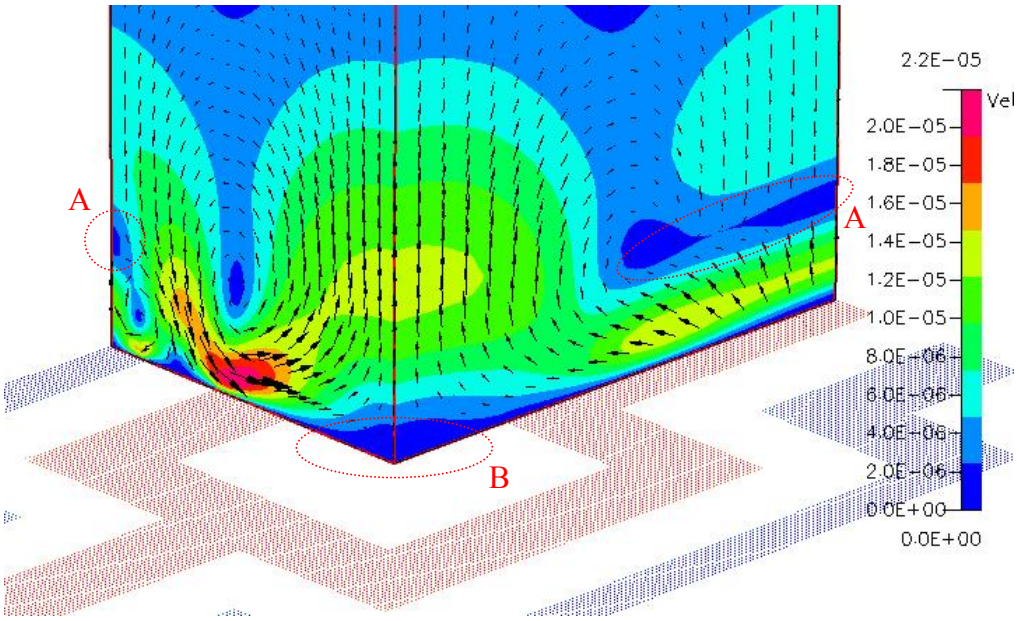

Figure 4.3 Electrothermal flow velocity distribution at the symmetry planes. Direction and magnitude of the flow velocity are presented as vector and contour plots, respectively. Two main stagnation zones are specified with red circles.

magnitude of the flow velocity are presented as vector and contour plots, respectively. A converging flow towards the center of the trapping zone can be observed on the square block. At the electrode gaps, counter vortices due to this flow are generated, creating complex local flows. Thus, the electrothermal flow motion produces several stagnation zones, which appear as low velocity magnitude regions. The maximum velocity appears to be 22 μm/s at the tip of electrode, making a flow roll above the electrode and transporting the fluid tangentially to a low electric field zone. This type

of flow has been reported in the literature for planar interdigitated electrodes with the utilization of two dimensional simulations.[74, 76] Since the width of the electrode is smaller than the length of its straight portion, similar flow structure is locally observed in the vicinity between the two parallel electrodes. These flow rolls are expected to occur along four sides of the square shape, and they generate flows towards the center of the trapping zone. Meanwhile, counter vortex pairs induce flow motions outside this main flow regime and a stagnation zone is created around 23 μm above the straight portion of the electrodes, which is specified as zone A in Figure 4.3. Due to its symmetric repetition, identical flow structure should exist on both regions entitled as zone A. The figure shows cross sectional views at two different planes. It can be observed that another large stagnation zone, specified as zone B, is created on the trapping zone due to the incoming flows from the four sides of the square electrode symmetrically. Particles are expected to move continuously to these stagnation zones by the hydrodynamic drag force of the induced flow. In the latter case (zone B), the trapping zone is under the effect of DEP forces that also drive particles in the same lateral directions, which means electrothermal motion does not interfere with DEP motion of particles. Moreover, DEP produces downward forces to trap particles inside the low electric field zone. Accordingly, trapping of particles inside this zone can be enhanced by the existence of active eletrothermal motion. In order to analyze the direction and effective range of the DEP trap, DEP force is numerically predicted. Figure 4.4 shows a numerical result of DEP force direction acting on 1 μm silica particles at 10 V amplitude and 10 MHz frequency. The planar

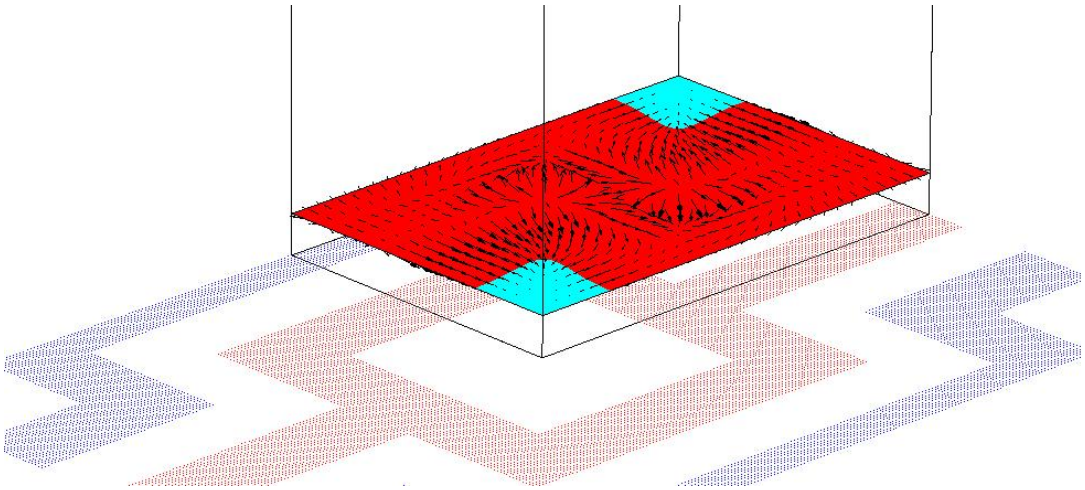

Figure 4.4 Numerical prediction of DEP force direction acting on 1 μm silica particles at 10 V amplitude and 10 MHz frequency. The planar components of DEP forces are plotted at a plane 11 μm above the electrode surface. Contour colors represent direction of the vertical component of DEP force (Red – upward, Cyan – downward).

components of DEP forces are plotted at a plane 11 μm above from the electrode surface. Contour colors represent the direction of vertical component of the DEP force (Red – upward, Cyan – downward). As can be seen on the figure, DEP pushes particles towards the trapping zone on the bottom surface with well-focused lateral force components. However, the directions of these forces are changing with particle positions and there are certain volumetric ranges where particles can be kept by DEP forces. Figure 4.5 shows this effective range of DEP trapping. The pink colored

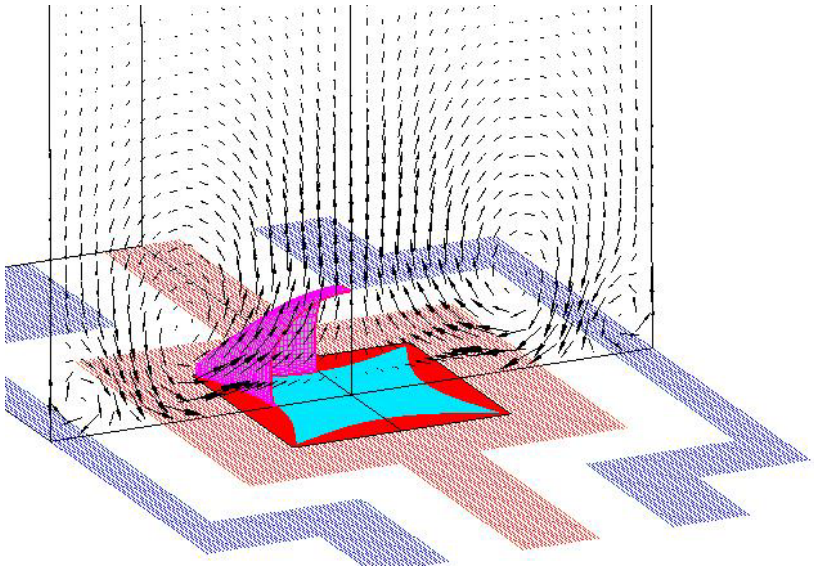

Figure 4.5 Electrothermal flow velocity distribution at the horizontal symmetry plane. Pink colored iso-surface represents effective DEP trapping zone determined by the direction of vertical component of DEP force. Inside this zone, DEP force pushes particles onto the cyan colored area at the bottom surface.

surface represents the effective DEP trapping zone determined by the direction of vertical component of the DEP force. Inside the volume enclosed by this surface, DEP force pushes particles onto the cyan colored area at the bottom surface. Effects of electrothermal motion can be seen from the flow velocity plotted in the same figure. As explained, the convective rolls along the sides of the square electrode create a converging flow towards the center of the trapping zone, and the particles are expected to be continuously transported to the DEP zone by lateral motions of the

flow. Vertical velocity of the electrothermal flow is very small inside the stagnation zone, as shown in Figure 4.3. As a result, trapped particles will not follow the flow stream and remain inside the surface by DEP forces. Hence, the induced electrothermal flow in the presented device is anticipated to enhance DEP particle trapping. In order to validate and utilize the results from the numerical simulations, experimental observations are conducted and summarized in the following section.

4.4 Experimental Results

A rectangular fluid chamber with 1 mm width was constructed by placing a 600 μm thick PDMS spacer along the electrodes array. Then, 1 μm silica particles (8100, Duke Scientific), suspended in 3.7 mM NaCl solution with 0.2 % mass fraction were pippeted into the chamber. After applying AC electric field at 10 V amplitude and 10 MHz frequency, particle distribution was recorded. Figure 4.6 shows trapped silica particles after applying the electric field for 5, 10, 20 and 30 min. Concentration of silica particles at the trapping zones was gradually increased with time. Unlike the previous experiments with a 10 mm diameter O-ring spacer in section 3, typical buoyancy driven flows did not appear in the observation period. This is due to use of a PDMS spacer with a smaller characteristic length. Instead, particles were concentrated to form clumps on periodic positions several seconds after applying the electric fields, as shown in the figure. Particles were also trapped inside the square blocks due to negative DEP forces. It can be observed that particle

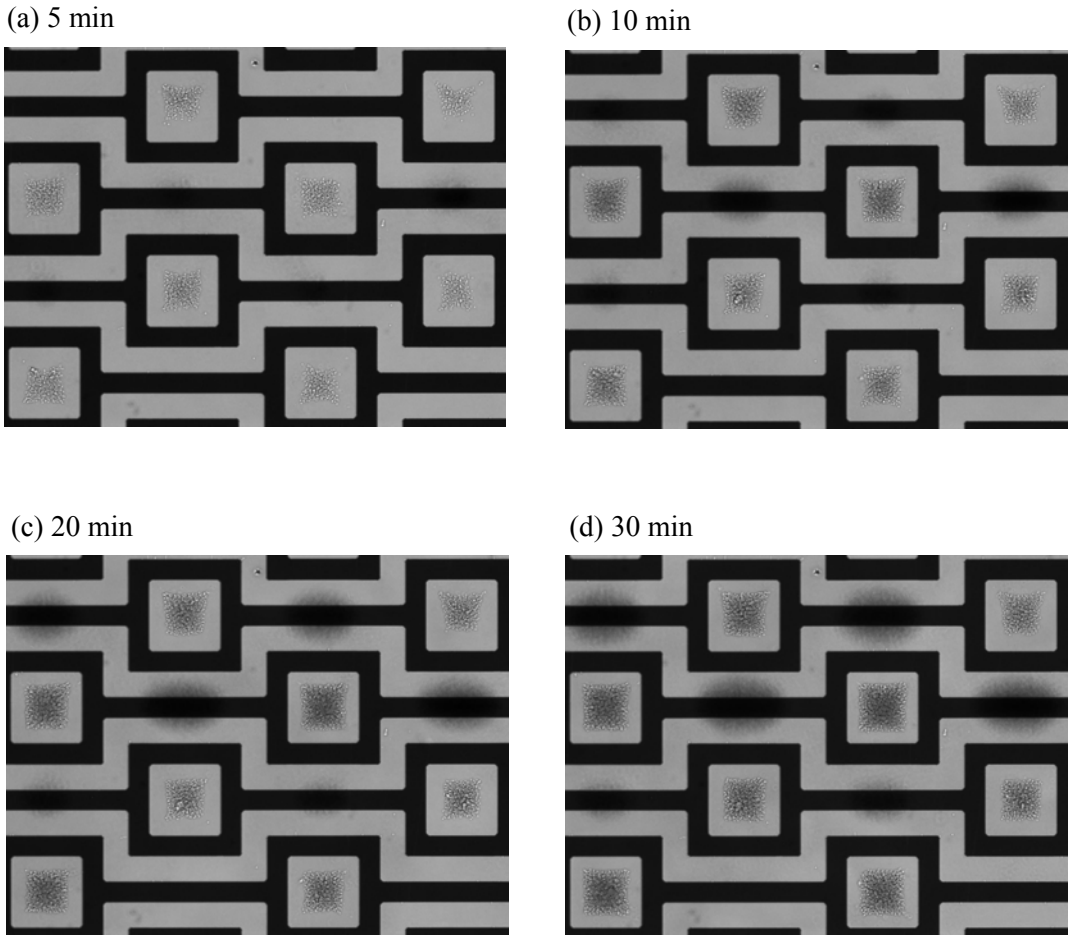

Figure 4.6 Image of 1 μm silica particles suspended in 3.7 mM NaCl solution (0.049 S/m) after applying AC electric field for (a) 5 min (b) 10 min (c) 20 min (d) 30 min at 10 V amplitude and 10 MHz frequency.

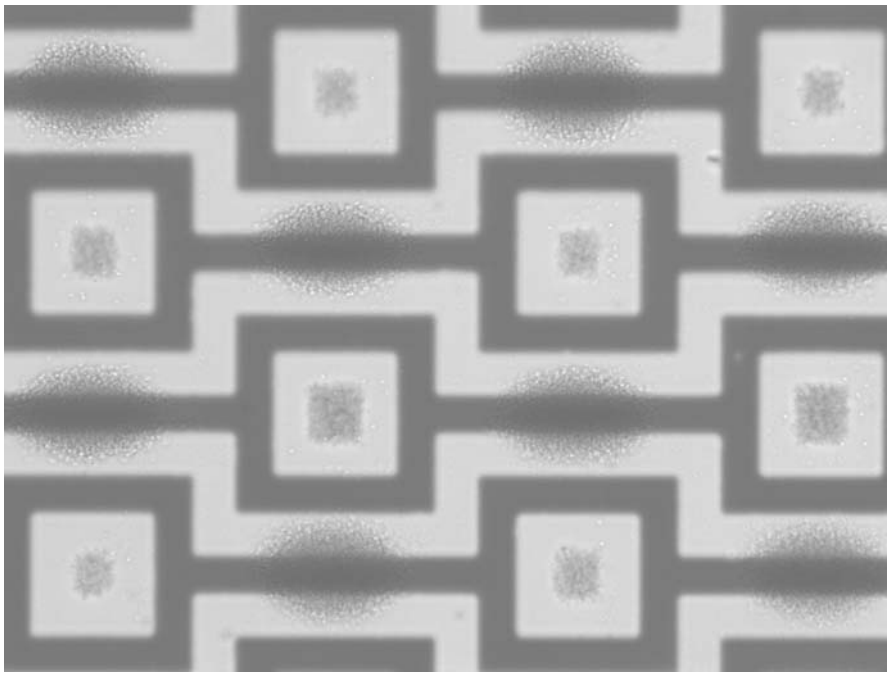

Figure 4.7 Image of 1 μm silica particles suspended 3.7 mM NaCl solution (0.049 S/m) after applying AC electric field at 10 V amplitude and 10 MHz frequency. Image was taken at 26 μm upper focal plane from the electrode surface.

concentration at both regions was increasing with time. The resultant distribution of particles and increase of particle concentration support the prediction of numerical simulations. Formation of particle clumps above the bottom surface is seen as the result of symmetric electrothermal fluid motion, providing force balance on the particles against gravity. The specific gravity of silica particles is 2.2 and the time scale of particle sedimentation is ~10^3 sec, which is comparable to the observation

time scale. This periodic formation of particle clumps inside a fluid volume also demonstrates the dominant electrothermal motion over the buoyancy driven flow. Since only a single stagnation zone along a symmetric line of the fluid chamber exists in the case of the buoyancy driven flow, it will disturb the periodic formation of particle clumps. Thus, it can be conjectured that the local circulatory motion of the fluid was induced by electrothermal effect, and particles were continuously driven to the stagnation zones and trapped, as depicted in Figure 4.3. Figure 4.7 shows aggregated particles at the equilibrium position inside fluid volume more clearly. The image was taken at a focal plane 26 μm above the electrodes. As shown in the figure, clusters of particles were formed in a symmetrical way and kept in the vertical position due to the balance of hydrodynamic and other forces. The distance of particle clusters from the bottom surface was measured approximately using a vertical movement of the microscope stage. This measurement was close to the position of the stagnation zone predicted by the numerical simulations at 23 μm. In order to observe the effect of this equilibrium distance, particle motion was monitored as the height of fluid volume was decreased. We slowly evaporated the fluid in the ambient condition without a cover glass, and the interface of water and ambient air was continuously dropped. Due to the large difference between electrical conductivity of water and air, electric field could be insulated inside a fluid volume. At the beginning of the experiment, particles showed similar movements as the previous cases. Particles were concentrated on two trapping zones and the concentration of trapped particles was gradually increased with time. However,

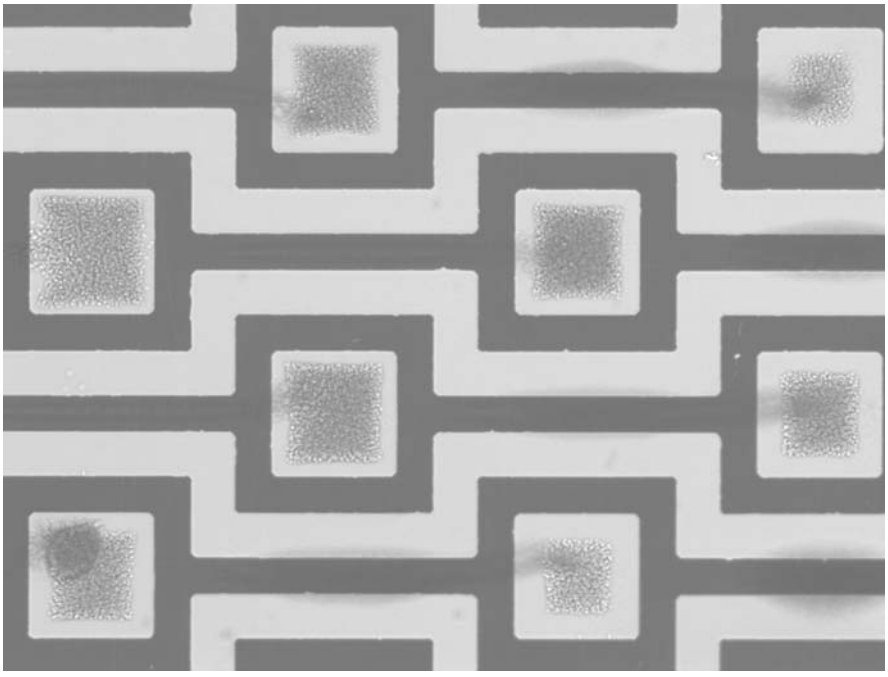

Figure 4.8 Image of 1 μm silica particle cluster break up and re-entrapment on the DEP traps. As the height of the liquid in the chamber was decreasing, released particles from the clusters above the electrodes were trapped inside the square blocks on the bottom electrode surface.

particle clusters floating above the electrodes started to break up as the fluid level was getting close to the equilibrium position. Since the stagnation zones were formed by interaction of flow rolls, a fluid chamber size should be high enough to maintain the flow structure and keep the position of the stagnation zones. As we decreased the height of upper boundary close to the characteristic flow roll size, flow structure was

disturbed and particle clusters were broken down. Particles released from the stagnation zones were trapped inside the square block by DEP force rapidly. Figure 4.8 shows the break up of particle clusters above the electrodes and their re-entrapment on DEP zones. Due to the shallow fluid volume, effective range of DEP trap relative to the whole volume was increased and particles were trapped inside the square zones efficiently.

4.5 Conclusions

Electrothermal flow motion on the square block electrodes and its effects on DEP trapping of colloidal particles are investigated. Flow structure induced by temperature gradients is analyzed using three dimensional simulations, and the DEP trapping enhancement due to the flow motion is explained. It is shown that convective rolls along the sides of square electrodes induce converging flows towards the center of the DEP traps and create a stagnation zone on the surface. Effective DEP trapping ranges are also predicted based on the DEP force directions. The numerical results indicate that particles are transported by electrothermal flows to the effective DEP region and trapped inside the square blocks by DEP forces. Experimental observations are performed to compare with the numerical results. Periodic structure of the electrothermal flow is validated by observing distribution of particle clusters trapped in the stagnation zones. It is shown that DEP trapping of particles is increased with time enhanced by the electrothermal flow in the experiments. The presented study shows electrothermal flows that often bring adverse effects on electrokinetic manipulations can be utilized to improve DEP trapping

efficiency. The possible enhancement of DEP manipulations with electrothermal effects will broaden the limit of electrokinetic manipulations in physiological media with high conductivities.

5. MICROFLUIDIC SAMPLE CONCENTRATION USING ULTRA SONIC STANDING WAVES

5.1 Introduction

Rapid detection of pathogens in food matrices, usually in the form of liquid samples, is an extremely challenging endeavor. It is a greater challenge when the pathogen is present either in extremely low numbers or in a form that is unrecognizable by conventional antibody based approaches. Over the past couple of years, there has been a variety of developments of specific, sensitive and high throughput technologies to detect pathogens in foods. However, the practical relevance of these technologies for actual deployment is still limited, and a key limitation of these technologies is linked to the small sample volumes that can be analyzed by the current methods (e.g., 5 μl).[77] Thus, without an adequate pathogen concentration step from relatively large volumes, many of these advanced technologies are severely limited.

Many conventional methods for sample concentration are available including solid-phase adsorption, aqueous two-phase partitioning, centrifugation, filtration, and immunomagnetic separation (IMS).[78] However, these methods generally require long processing time with well supervised operation, and are not free from costs of special equipments and labor inputs. Moreover, integration with molecular diagnostic devices is very limited. On the other hand, microfluidic techniques based on a micrometer scale device can be used effectively for concentrating small size particles including biological species.[79] Conventional microfabrication techniques allow cost effective, or even

disposable devices, and the small foot print area of these devices enable their integration with other diagnostic components, allowing fully automatic analytical processes.[80]

Among the many manipulation techniques in microscale, ultrasonic standing wave (USW) offers a non-contact mode of particle handling, which makes it an attractive tool in biological species handling microsystems, since minimum mechanical stress is induced by the applied acoustic forces.[81] Utilization of USW is increasingly effective as device dimensions decreases to microscale, and such small devices can be readily integrated with other functional components with simple and inexpensive fabrication methods. The most important advantage of USW manipulation is that particles can be controlled in predictive manner without identifying their positions, whereas other non-contact methods, *e.g.* electromagnetic and optical, can be applied only in a point-wise manner. This characteristic of USW manipulation is very well suited with the sample concentration task, which requires simple and fast aggregation of target species from suspending media.

Particles suspended in a liquid medium and subjected to USW experience an axial direct radiation force (DRF) that is induced by a time-independent acoustic potential energy field.[82] DRF that drives redistribution of the particles in a medium can be derived from the particle potential energy expression as[83,84]

$$DRF = -\frac{\pi P^2 V_p \beta}{2\lambda} \cdot \phi(\beta, \rho) \cdot \sin\left(\frac{4\pi z}{\lambda}\right), \tag{5.1}$$

where P is the sound pressure amplitude, V_p is the particle volume, λ is the wavelength of the driving signal, z is the distance from the pressure node, β is the compressibility

(β=1/ρc^2), ρ is the density, c is the speed of sound, ϕ is the contrast factor, given by $\phi = (5\rho_p - 2\rho)/(2\rho_p + \rho) - \beta_p / \beta$, and subscript p refers to the particle. In the presence of DRF, particles initially suspended in a medium move and concentrate to the position where the particle potential energy can be minimized, as illustrated in Figure 5.1. Particles are driven to the pressure nodes for $\phi > 0$, while $\phi < 0$ causes movement to the anti-node.

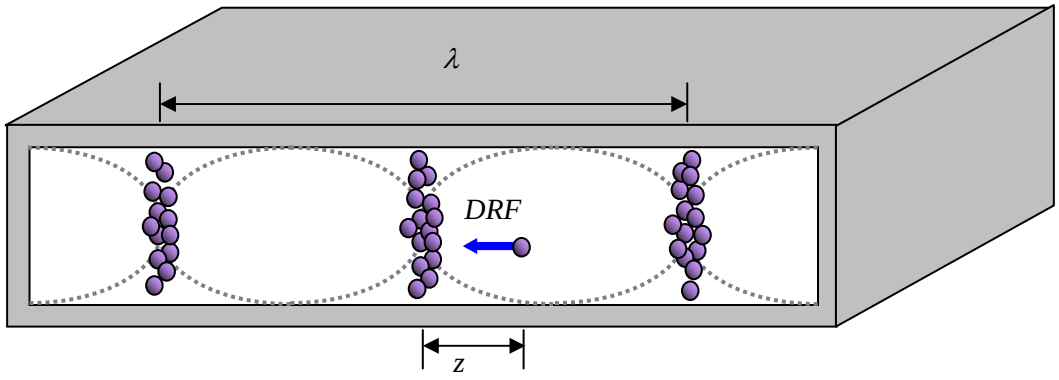

Figure 5.1 Schematic of particle motion under the influence of USW created inside a microchannel.

Acoustic manipulation of colloidal particles has been proven as an effective and fast method, and it has been used for separation of suspended particles from their media by several researchers. However, most of previous demonstrations were based on millimeter scale devices.[85-87] Only a small number of studies have been reported for particle separation and sorting with fluidic channels of few hundred micrometer width.[88-91] Recently, there is an increased interest of scaling down the fluidic channels to a size of tens of micrometers. By reducing the channel width, particles are expected to be focused on narrower bands of pressure nodes or antinodes, because the acoustic force acting on the particles increases with higher resonance frequency inside the microchannel.[88] Accordingly, separation efficiency can be improved by confining the particles into a smaller space. Working with high frequency acoustic wave is also advantageous for avoiding cavitations inside the channel device. Moreover, advancement of microfabrication techniques allows fabrication of the high-frequency acoustic resonators with adequate precision.

In this section, USW manipulation of colloidal particles is experimentally investigated, and a continuous microfluidic system that enables high throughput sample concentration based on long-range DRF force is tested. An acoustic resonator is constructed using a microchannel of 50 μm width, which allows high frequency resonance modes. Also, the microfludic system is built on a single glass channel. Due to the low acoustic resistance and ease of fabrication, many of previous researches utilized an acoustic resonator on a silicon wafer.[88-90] However, the silicon device requires a glass plate at the top surface of a channel for visual inspection, therefore using silicon/glass

device could cause undesirable asymmetric acoustic coupling. In order to avoid non-uniform acoustic reflections, we fabricated the resonator using a single material. Overall responses of particles in a continuous microfluidic system are investigated with experimental observations, and then the performance of a unit device is analyzed. Additionally, integration of multiple channels to increase the volumetric capacity and the concentration efficiency is discussed.

5.2 Methods and Materials

Schematics of the current device along with its photograph are shown in Figure 5.2. USW was created inside a suspending medium by attaching a rectangular ultrasonic transducer (Boston Piezo-optics, MA) on top surface of the glass microchannel with height of 20 μm and width of 50 μm (MC-BF4-SC, Micralyne). A PCB board was used to hold the channel and make electrical connections. Syringe pump (PHD 22/2000, Havard Apparatus) was connected to an inlet port of the channel to feed 1 μm fluorescent polystyrene particles (FluoSpheres, Interfacial Dynamics). The particle concentration was adjusted to 1×10^8/mL approximately from a manufacturer's solution with DI water (Simplicity, Millipore). 84 V peak-to-peak AC voltage was supplied by a function generator (AFG 3102, Tektronix) and a RF amplifier (TIA-1000-1R8, Mini-Circuits) in the frequency range of 0~100 MHz. Particle motion was observed using an optical microscope (TE2000-U, Nikon) and a 40X objective (0.6 NA). Images were captured using software (Image Pro, Media Cybernetics) and a CCD camera (PowerView1.4MP, TSI) with 1376 × 1040 pixel resolution (6.45 μm pixel size).

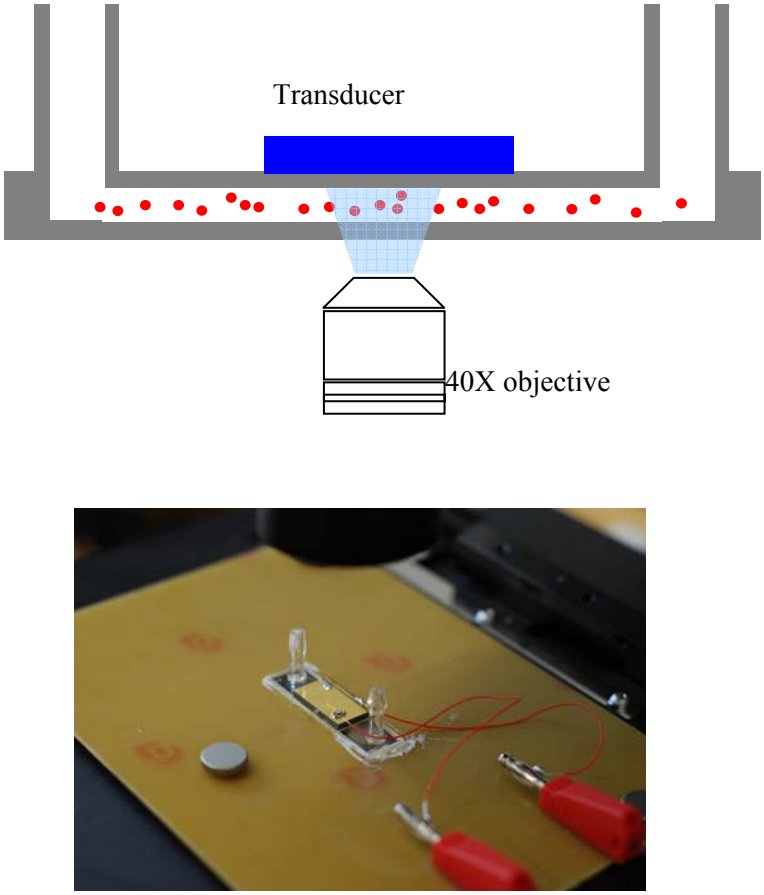

Figure 5.2 Schematics and a photograph of the device used for USW experiments. Ultrasonic transducer was attached on the top of the micro-channel to create USW, and a PCB board was used to hold the channel and make electrical connections.

5.3 Results and Discussion

5.3.1 Single Channel Device

Figure 5.3 shows particle distribution inside the glass microchannel under the influence of USW. Particle suspension was acoustically actuated by a piezoelectric transducer. Although the acoustic signal was propagated from the top surface of the channel, standing waves were obtained parallel to the top plane and orthogonal to the main flow direction. Since contact area of the transducer was much larger than the top surface of the channel, overall channel volume was uniformly actuated and horizontal standing waves were created due to the low aspect ratio of the channel cross section. In order to find a resonance condition, frequency was gradually increased and the first resonance mode was found at 14.11 MHz, as shown Figure 5.3b. As USW was created inside the channel, particles were aggregated at pressure nodes and a single band was formed in the middle of the channel. The second resonance mode was found at 27.20 MHz, as shown in Figure 5.4. Two particle bands were formed around $\lambda/4$ and $3\lambda/4$ lateral positions. Compared with the first resonance mode, particle streams were not clearly focused. This is mainly due to the cross-sectional shape of the channel with rounded corners, which is a typical profile of isotropic wet-etching. As the pressure nodes were formed near these corners, the node positions were varied along the depth-wise direction, and overall width of particle bands was seen to be increased. The local effect of this geometric variation can be avoided by making a rectangular cross section with sharp corners, which can be done using anisotropic etching methods.

Once particles are concentrated, collection of concentrated particle suspensions

(a)

(b)

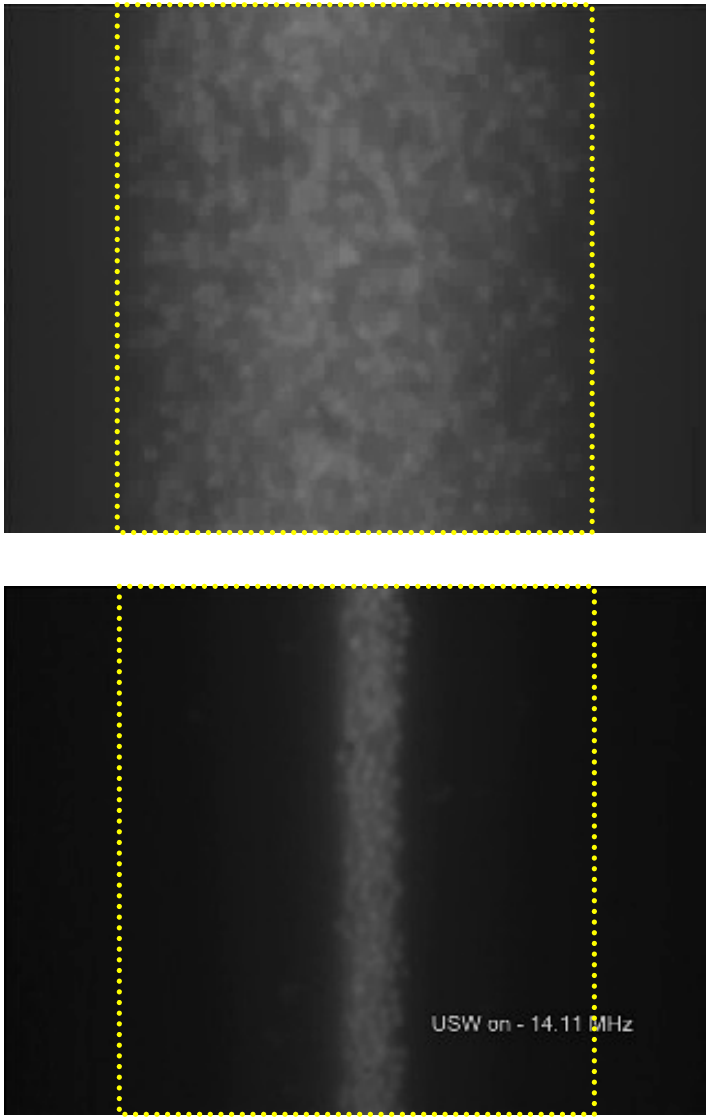

Figure 5.3 Fluorescent images of 1 μm polystyrene particles suspended in DI water (a) Particle distribution under pressure driven flow (b) Particle concentration after applying 14.11 MHz USW. Dashed lines are added to images for identification of the wall boundaries.

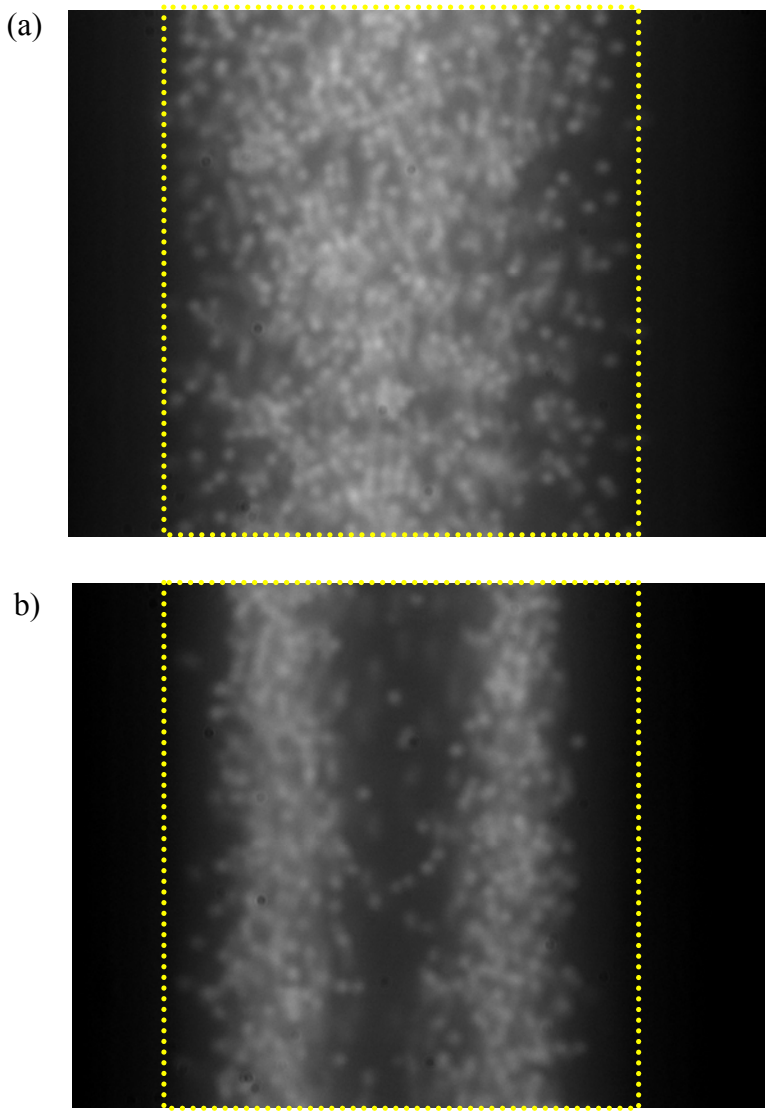

Figure 5.4 Fluorescent images of 1 μm polystyrene particles suspended in DI water (a) Particle distribution under pressure driven flow (b) Particle concentration after applying 27.20 MHz USW. Dashed lines are added to images for identification of the wall boundaries.

can be easily done by a flow field fractionation (FFF) technique that utilizes split outlets with different width.[81] The concentration efficiency can be expressed using the ratio of inlet and outlet concentration values as

$$CR = \frac{C_{out}}{C_{in}}. \tag{5.2}$$

Since laminar flow prevails due to low Reynolds number in the microchannel, particles will remain in their lateral positions even after leaving the actuation area until they reach the end of the channel with different outlets. Thus, the maximum concentration ratio can be calculated using the width of the channel inlet, *w*, and the width of the particle bands, δ, as

$$CR_{\max} = \frac{w}{n\delta}, \tag{5.3}$$

where *n* is the number of particle bands. Based on a pixel data measurement of recorded images, an average width of the concentration band was found as 7.5 μm and concentration ratio was calculated as 670 % at the first resonance mode, *n*=1. The maximum concentration ratio can be increased with smaller value of δ. For the purpose of visual inspections, a large number of particles were used in the experiment, and a dense concentration band was formed. However, particles will be positioned on pressure nodes without interfering each other in case of low particle concentration, which will be usual inlet condition of concentrators. Figure 5.5 shows the concentration of *C. sporogenes* bacterial spores using the first resonance condition. Because of the lower

(a)

(b)

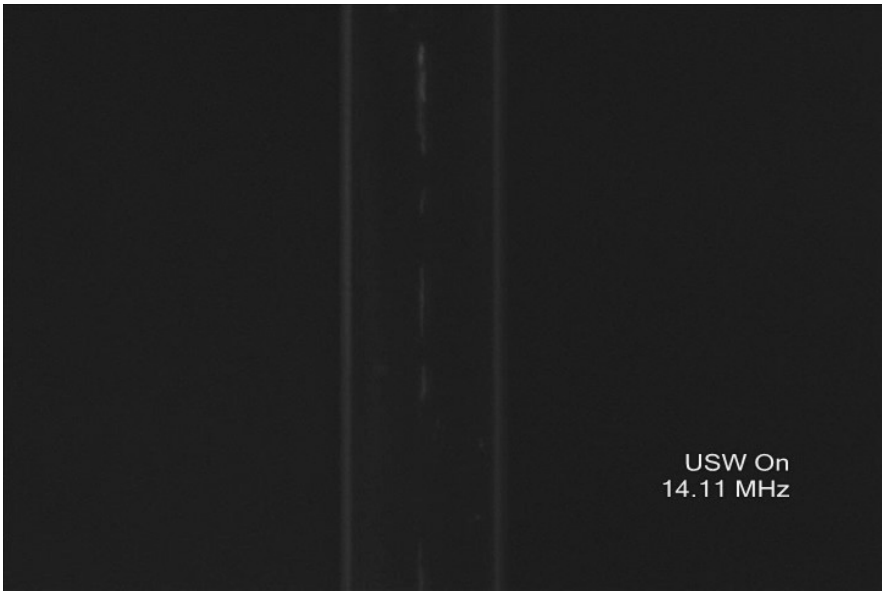

Figure 5.5 Fluorescent images of *C. sporogenes* suspended in DI water (a) Spore distribution under pressure driven flow (b) Spore concentration after applying 14.11 MHz USW.

concentration (~10^7/ml), a dense particle band was not observed. Instead, a single particle streak well aligned on a pressure node was formed. The resultant concentration ratio was not measured with image analysis because of low resolution of the images. However, we expect that the concentration ratio will be higher compared with the dense colloidal suspension case due to the narrow band formation. For evaluation of the concentration efficiency, direct measurement of the spore concentration at split outlets will be required.

In order to predict performance of the current device as a function of the operational variables, experimental results were correlated with theory. Assuming quasi-steady state with force equilibrium between DRF and Stokes drag, the lateral velocity of particles can be expressed as

$$u_{DRF} = \frac{\pi a^2}{18\eta} \beta P^2 \phi \frac{n}{w} \sin\left(\frac{2\pi n z}{w}\right), \tag{5.4}$$

where a is the particle radius, η is the fluid viscosity. The lateral velocity of the particles is proportional to the square of acoustic pressure, the order of resonance, and the inverse of channel width. The lateral motion of particles due to DRF should be large enough to induce an effective particle concentration at pressure nodes, dominating diffusive motions of particles. This can be achieved by increasing the acoustic pressure or operating at high order of resonance mode in a narrow channel, which means a high frequency operation (f=(c/2)·(n/w)). The dominance condition of USW motion can be found by comparing the magnitudes of particle displacements per unit time induced by DRF and Random Brownian motion, which are X_{DRF} and $X_{Brownian}$, respectively. Using

the expression of Random Brownian motion of a particle in one dimension, given as equation 2.12, and the DRF lateral velocity, the condition for dominant USW motion can be expressed as

$$\frac{\pi a^2}{18\eta}\beta P^2 \phi \frac{n}{w} > \left(\frac{k_B T}{3\pi a \eta}\right)^{1/2}. \qquad (5.5)$$

At the first resonance mode, the maximum particle velocity was calculated as 18 μm/s using particle tracking image analysis code (ImageJ, NIH). The contrast factor, ϕ, was computed using the properties of polystyrene particle and DI water, which are ρ_p=1050 kg/m^3, c_p=3000 m/s, ρ=1000 kg/m^3, and c=1498 m/s.[92] The resultant acoustic pressure was 0.2389 MPa. Figure 5.6 shows calculated trajectories of particles as a function of time based on the values. With the assumption of force equilibrium and negligible inertial effect of small particles, transient lateral motion of particles was predicted using the computed particle velocities at different initial positions. Figure 5.7 shows a phase diagram predicting the dominant transport mechanism as a function of the particle radius and the channel width at this condition. For 1 μm polystyrene particles suspended in DI water at room temperature, the magnitude of Brownian motion displacement was calculated to be two orders less than the DRF displacement, supporting the dominant USW motion in the experiment. However, it can be seen that DRF becomes less effective if the channel width is increased to ~1 mm. Thus, selection of larger channel width to achieve high concentration ratio is limited.

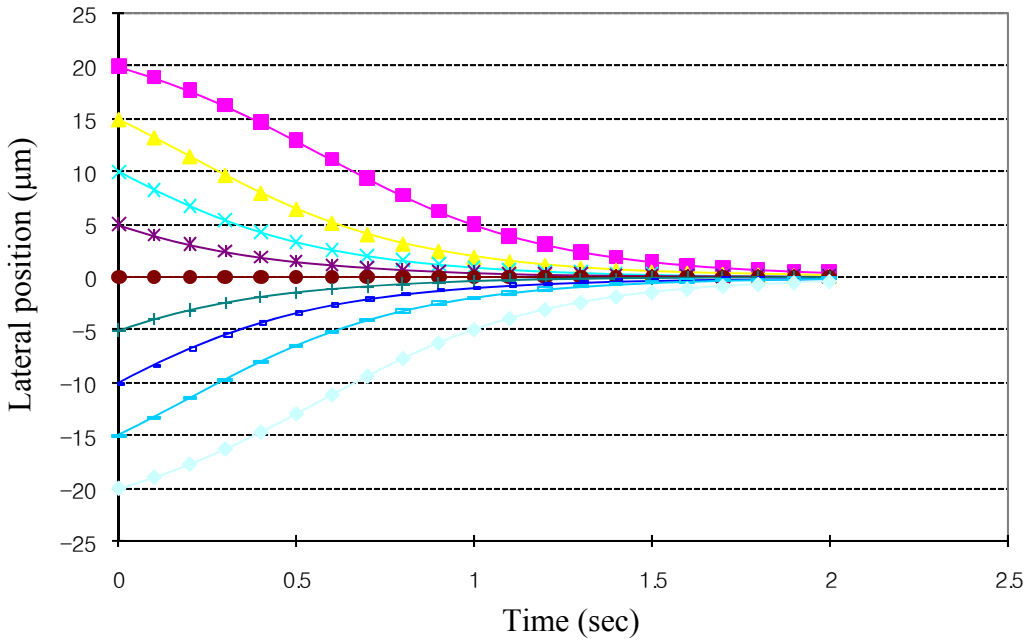

Figure 5.6 Trajectories of 1 μm polystyrene particles actuated with USW at the first resonance mode inside a 50 μm microchannel. Transient lateral positions of particles are calculated based on the assumption of quasi-steady state with force equilibrium between DRF and Stokes drag.

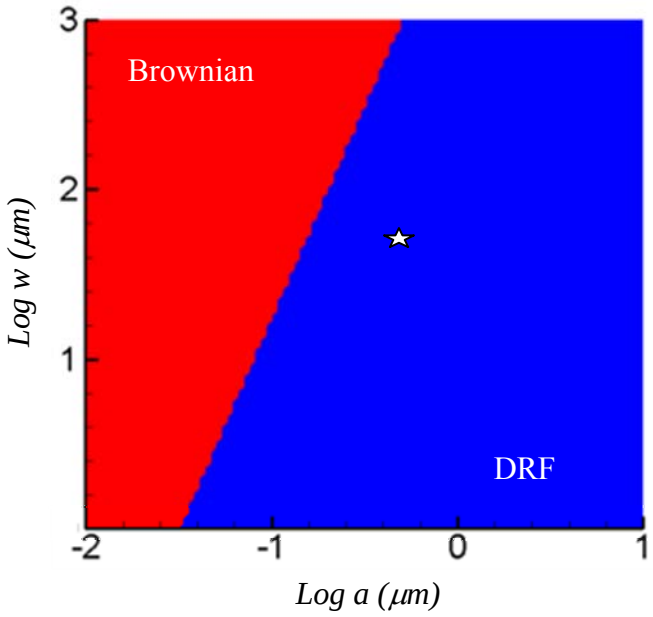

Figure 5.7 Particle radius-channel width phase diagram for polystyrene particles suspended in DI water (for ρ_p=1050 kg/m^3, c_p=3000 m/s, ρ=1000 kg/m^3, c=1498 m/s, T= 300 K, and P=0.2389 MPa). The values that correspond to the experimental conditions are specified with a star (a=0.5 μm and w=50 μm).

The concentration ratio can be improved by minimizing the width of particle band. If particles are aligned on a single pressure node line exactly, δ should be same as particle diameter, and the concentration ratio should have its maximum value, $w/2a$, with the outlet width of $2a$. However, diffusive motions of particles generally induce lateral fluctuations after particles are aligned at pressure nodes. Thus, actual width of particle bands can be expressed using the Random Brownian motion term as

$$a + \left(\frac{k_B T}{3\pi a \eta} t \right)^{1/2} \leq \delta / 2 \tag{5.6}$$

In case of 1 μm particles suspended in water at room temperature, the increase of the particle band width is not significant, because the magnitude of Brownian motion is approximately one order less than the particle size. If the particle size is decreased, the diffusive motion of particles can be magnified, while DRF decreases proportional to the square of the particle radius. Therefore, amplification of DRF is necessary as particle size decreases, by increasing either the acoustic pressure or the frequency. Since DRF and hydrodynamic force of pressure driven flow induce lateral and axial motions of particles, respectively, migration of the particles to specific positions within the flow motion is limited by these two forces. Required time to concentrate particles along the single pressure node is $(\lambda/4)/u_{DRF}$, and the particle residence time within the acoustic actuation length L is L/u_{PDF}. In order to achieve the maximum concentration ratio, the migration time of particles to the pressure node should be shorter than the particle residence time. Thus, the flow rate limit to achieve the maximum concentration ratio can be determined from the condition, $L/u_{PDF} \geq (\lambda/4)/u_{DRF}$, as

$$Q_{\lim} = \frac{1}{9} AR \frac{\pi a^2}{\eta} \beta P^2 \phi L n^2 \ \ (\textit{for the maximum CR}) \tag{5.7}$$

where AR is the channel aspect ratio (height/width), L is the actuation channel length. If the flow rate exceeds this limit, concentration ratio decreases due to insufficient focusing of particles to a collection zone. Using the maximum lateral velocity for calculating the lateral displacement, X_{DRF}, the concentration ratio can be expressed as

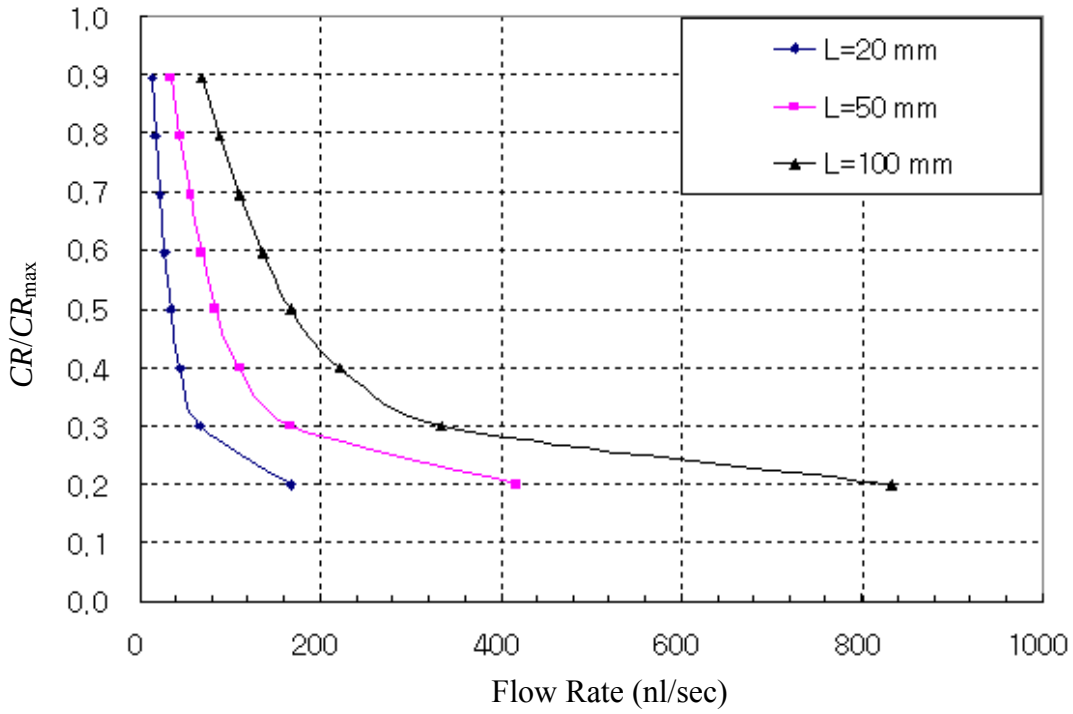

Figure 5.8 Normalized concentration ratio at the first resonance mode as a function of flow rate and acoustic actuation length for a single channel device. Channel cross section area is 50 μm × 20 μm.

$$CR = CR_{\max}\left(1 - \frac{2X_{DRF}}{\lambda/2}\right) = CR_{\max}\left(1 - \frac{Q_{\lim}}{Q}\right) \ (for\ Q > Q_{\lim}). \qquad (5.8)$$

Based on the result of particle trajectories, the concentration ratio was predicted as a function of a flow rate, as shown in Figure 5.8. Different acoustic actuation lengths of the channel were used for the calculation as specified in the figure, and the δ was assumed to be 7.5 μm at the first resonance mode. The concentration ratio is inversely

proportional to the flow rate in case of a fixed channel length, and thus increase of flow rate over the limiting value is restricted with target concentration ratio of the unit device. Otherwise, the channel length should be increased linearly with the flow rate for maintaining the maximum concentration ratio in the single channel device.

5.3.2 Multiple Channel Device – Design Parameters

Performance of sample concentrators can be determined based on two key parameters, the maximum concentration ratio and the flow rate. It is required to achieve a sufficient concentration ratio for obtaining the proper concentration of analytical samples in a range of detection limit. The volumetric capacitance of the device becomes important for the application that requires the processing of large sample volume. One possible way of overcoming the limited performance of a single channel device is to integrate several unit devices on a chip, which is a typical advantage of microfluidic systems. Two methods of device integration are shown in Figure 5.9. Serial connection of multiple channels, as shown in Figure 5.9a, can be utilized for increasing the concentration ratio. At each channel, sample concentration is increased with the designed ratio, CR, while the flow rate of the integrated device is maintained same as a single channel device. The concentration ratio of the device integrated with N channels in this manner can be expressed as $CR_{tot}=(CR)^{N}$. Figure 5.9b shows parallel connection of multiple channels. Since operating condition is identical at each channel, the concentration ratio is not changing from the value of the single channel device. However, total flow rate can be linearly increased with the number of the channels as $Q_{tot}=NQ$,

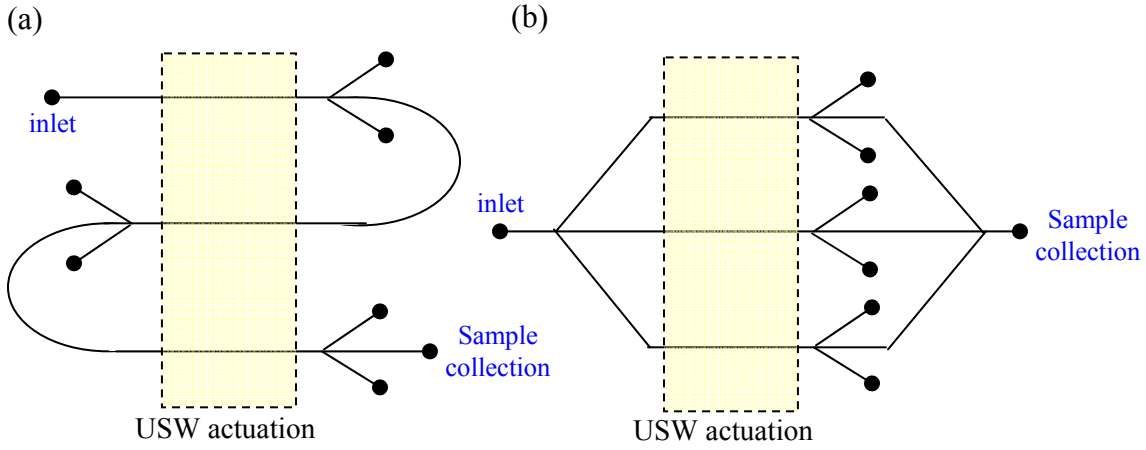

Figure 5.9 Schematics of (s) serial and (b) parallel integration of unit devices.

where Q is the designed flow rate for each channel. Additionally, the combination of these methods will be possible to exploit advantages of large flow rate and high concentration ratio at the same time.

For design and optimization of chip scale devices with multiple channels, system parameters are modeled based on the results of a single channel device, as summarized in Table 5.1. Design variables include width (w) and length (L) of a single channel, the order of resonance or the number of particle streams (n), the number of serial connections (NS), and the number of parallel connections (NP). Fixed variables are the aspect ratio of a single channel (AR), acoustic variables (δ, P), material properties (β, ϕ, η) and particle size (a). The aspect ratio of a channel, AR, can be selected as the highest value that allows creation of standing waves but prevents two-dimensional wave

Table 5.1 System parameters for a chip scale device

Design variables	w, L, n, NS, NP
Fixed variables and constraints	AR, δ, β, P, ϕ, η, a Resonance Condition : $f=cn/2w$ USW Dominance : $X_{DRF} = \frac{\pi a^2}{18\eta}\beta P^2 \phi \frac{n}{w} > \left(\frac{k_B T}{3\pi a \eta}\right)^{1/2}$
Target variables	$CR_{\max} = \left(\frac{w}{n\delta}\right)^{NS}$, $Q_{\lim} = NP\left(\frac{AR}{9}\frac{\pi a^2}{\eta}\beta P^2 \phi\right) L n^2$

propagations. The design variables can be determined to maximize the target variables, or achieve required performance. For example, the concentration ratio of the device can be improved by increasing the channel width and decreasing the number of particle bands, or making a serial connection of multiple channels. At same time, the control of the design variables for maximizing the concentration ratio is restricted. Increase of the channel width can induce decay of DRF, and the operations at low order resonance modes are inefficient for maximizing the flow rate. Integration of a large number of channels requires a complicated fabrication process. Thus, many strategies for optimizing the device performance can be existed. Based on various design goals, this parametric model can be actually correlated with experimental results and utilized in the development of integrated devices, providing the performance prediction with selected physical parameters. However, a further improvement of the model would be desired to

describe effects of the design variables in detail. A major modeling challenge is the precise characterization of acoustic actuation sources including acoustic pressure, *P*. Since USW distribution inside colloidal suspensions depends on the coupling of mechanical vibration of the channel wall and the piezoelectric transducer, modeling of wave propagation through the channel structure is required. In addition, the effect of secondary forces on particles, *e.g.*, streaming potential effects[84], needs to be explored especially in the case of a larger channel dimension or considerable heat dissipation due to high voltage operations. Besides the effect of design variables on the device performance, efficiency of device fabrication is the other important issue to consider. The utilization of high order resonance modes requires a large number of split outlets, increasing as (2*n*+1). The length of a single channel is also limited by available size of the piezoelectric transducer.

5.4 Conclusions

Utilization of USW for concentrating particles from their suspending medium is demonstrated in a continuous microfluidic system. High frequency actuation suitable for miniaturization of devices is successfully applied, and the unit device performance and key parameters are explained. By acoustically actuating colloidal suspensions, particle streams focused at pressure node lines are obtained using 14.11 MHz and 27.20 MHz frequency within a glass microchannel of 50 μm width. At the first resonance mode, sample concentration ratio is expected as 670 %. The concentration efficiency as a function of the flow rate is theoretically explained using the parameters correlated with

the experimental results. Based on the results of a single channel device, system parameters for the design of chip scale devices are modeled. The parametric model can be actually correlated with experimental results and utilized in the development of integrated devices, providing the performance prediction with various physical parameters.

6. SUMMARY

6.1 Summary of Conclusions

The overall goal of this research work is to develop microfluidic tools for manipulation and control of colloidal particles, which can be integrated and implemented on LOC systems. Two key mechanisms, electrokinetic and acoustic, are investigated and successfully employed in the microfabricated devices. First, electrokinetic mechanism is explored as a versatile colloidal manipulation method for standard analytical operations (*e.g.*, sample handling, separation and detection). The potential use of electrokinetic method for biosensor based detection is demonstrated with the DEP device for trapping of particles and biological species from the suspending media. Second, USW is demonstrated as an efficient tool for continuous sample concentration, allowing the automation of a common prerequisite step of sample preparation.

In section 2, AC electrokinetic motion of colloidal particles subjected to a spatially non-uniform AC electric field are examined using a simple theoretical model that considers the relative magnitudes of dielectrophoresis, electrophoresis, AC-electroosmosis, and Brownian motion. Dominant electrokinetic forces are explained as a function of the electric field frequency, amplitude and conductivity of the suspending medium for given material properties and geometry. Parametric experimental validations of the model are conducted utilizing interdigitated microelectrodes with polystyrene and gold particles, and Clostridium sporogenes bacterial spores. The theoretical model

provides quantitative descriptions of AC electrokinetic transport for the given target species in a wide spectrum of electric field amplitude and frequency, and medium conductivity.

Based on the solid understanding of AC electrokinetic forces, a microscale electrode for trapping bacterial spores from high conductivity food sample matrices is presented in Section 3. With a simple planar electrode having well defined electric field minima that can act as the spore attachment/detection sites for integration of biosensors, we utilize negative DEP to capture Clostridium sporogenes on patterned surfaces in a microfabricated fluid chamber. The electrode design is applicable for fast and effective patterning of biological species from high conductivity media including food sample matrices and physiological buffer solutions.

In section 4, electrothermal flow motion on the square block electrodes and its effects on DEP trapping of particles are investigated. Flow structure induced by temperature gradient is analyzed using three dimensional simulations. DEP trapping enhancement due to flow motion is explained. The periodic structure of electrothermal flow and stagnation zones are validated by experimental observations of particle clusters suspended at equilibrium positions. Electrothermal flows that often bring adverse effects on electrokinetic manipulations are successfully utilized to improve DEP trapping efficiency. Possible enhancement of DEP manipulations with electrothermal effects will broaden the limit of electrokinetic manipulations in physiological media with high conductivity.

In section 5, USW is employed for continuous sample concentration in a microfluidic device. Comparable advantages of USW over electrokinetic manipulations are explained including fast response and high throughput operations with long-range DRF. High frequency actuation suitable for miniaturization of devices is successfully applied and the device performance and key parameters are explained. At the first resonance mode, sample concentration ratio is expected as 670 %. Experimental results are correlated with theory, and the concentration efficiency as a function of the flow rate is explained. Based on the results of a single channel device, system parameters for the design of chip scale devices are modeled.

6.2 Future Research

The dissertation described efficient manipulation techniques of colloids in a microscale, specifically for capturing, patterning, and concentrating. Each technique can be further developed and optimized for specific applications. For example, electrokinetic response of various species can be modeled in detail and capturing efficiency of the device can be improved in a customized manner. At same time, the developed electrokinetic and acoustic methods can be integrated with each other or with other microfluidic techniques for diverse applications of LOC systems and material science.

Specifically, the presented microfluidic techniques can be integrated for the development of a small-scale chip with bio-analytical functionality. Site-specific capturing ability of the DEP device is readily applicable for integration of detection device, *e.g.*, anti-body surface, as illustrated in Figure 6.1. Meanwhile, fast aggregation

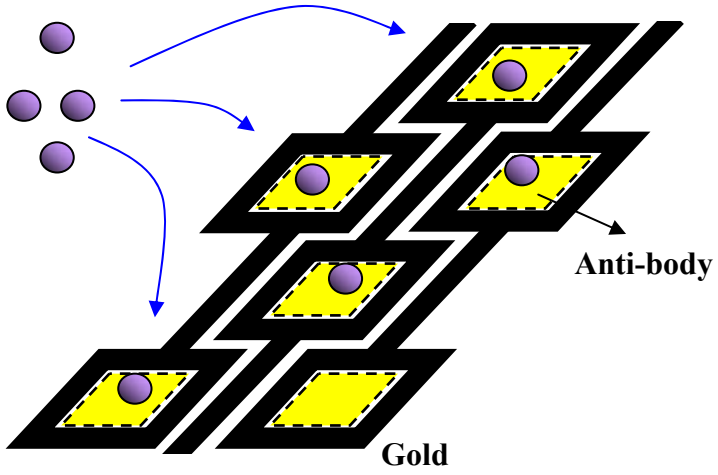

Figure 6.1 Schematic of DEP trap integrated with anti-body based detection surface.

of colloidal particles in the presence of USW is well suited for in-line sample pre-concentration. Thus, the integrated device will enable on-site detection of target species because a pre-concentration step with USW and FFF technique increases detection limit of the device while DEP trapping realizes specific attachment of the species on sensor surfaces.

As an important part of future research, it should be stressed that colloidal manipulation methods developed in this dissertation offer a promising route to self or directed assembly of colloidal crystals. Colloidal crystals are periodic structures made from micrometer and sub-micrometer particles suspended in media. Colloidal crystals received significant attention for fabrication of functional materials in a wide range of applications, such as optical coatings and filters,[93-95] photonic band gap (PBG)

materials,[96-98] nanolithographic masks,[99, 100] porous materials,[101, 102] and biochemical sensors.[103, 104] Using a self-assembly technique only, it is difficult to achieve the formation of non-close packed 2D and 3D arrays of colloidal particles and the deposition of complex patterns. Thus, additional mechanisms are generally required to increase controllability of the assembly process. Preliminary experimental results have demonstrated a feasible method for fabricating patterned colloidal crystals using electrokinetic mechanisms. Figure 6.2 shows colloidal assemblies immobilized on substrates using DEP and attractive capillary forces. Fast aggregation of colloidal particles into patterned geometry was induced by DEP and the colloidal assemblies were packed and immobilized on a substrate by capillary forces during a drying process.

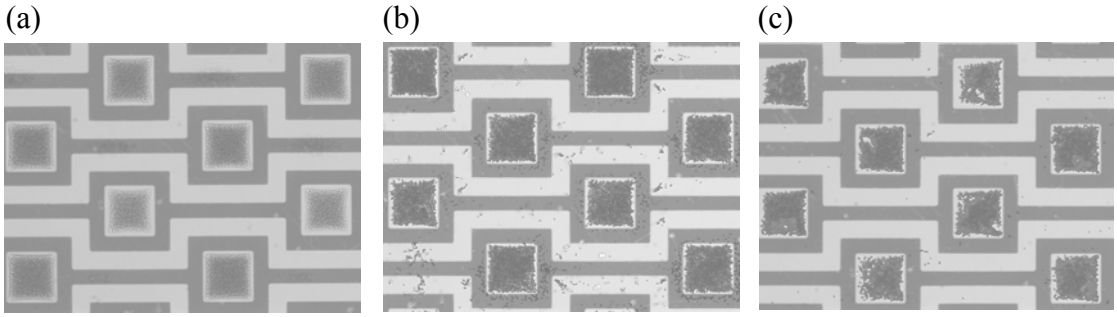

Figure 6.2 Images of 1 μm silica particles suspended in 3.7 mM NaCl solution (a) after applying AC electric field at 10 V amplitude and 10 MHz frequency (b) after evaporating the solution (c) after washing out with DI water.

Another initial study on selective assembly of binary colloidal mixtures also opens the possibility of fabricating a crystal structure other than face-centered-cubic shape. Figure 6.3 shows results of the experiments for changing the composition of binary colloidal assembly. Selective actuation of colloidal aggregation is possible utilizing different dielectric responses of particles. In order to achieve the binary structure with controlled order, precise characterization of the structure with consideration of transient interactions of polarized particles is required.

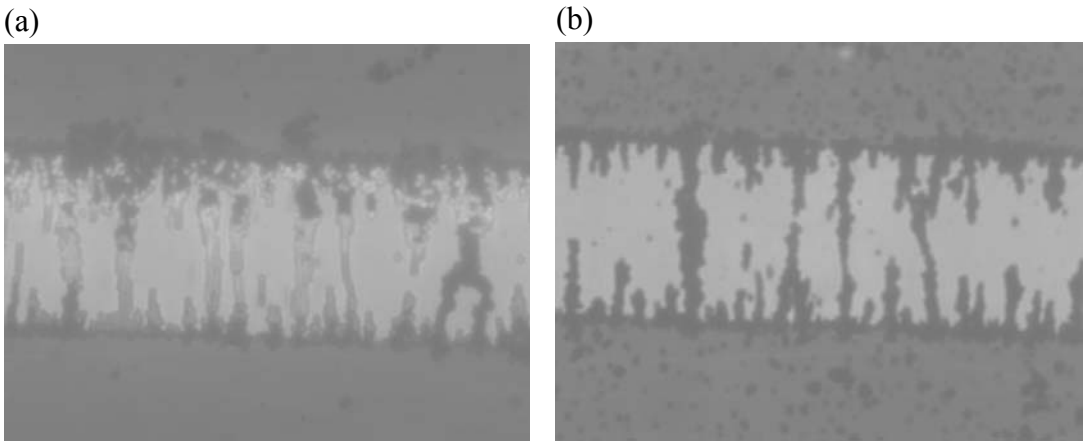

Figure 6.3 Images of 800 nm gold particles (dark spheres) and 1 μm polystyrene (bright spheres) suspended in DI water after applying AC electric field at 5 V amplitude and (a) 100 kHz (b) 5 MHz frequency. Different colloidal structures are formed between two planar parallel electrodes with 30 μm separation.

REFERENCES

1 Whitesides, G. M. *Nature* **2006**, 442, 368.

2 Stone, H. A.; Stroock, A. D.; Ajdari, A. *Annu. Rev. Fluid Mech.* **2004**, 36, 381.

3 Squires, T. M.; Quake, S. R. *Rev. Mod. Phys.* **2005**, 77, 977

4 Ali, E. J.; Sorger, P. K.; Jensen, K. F. *Nature* **2006**, 442, 403.

5 Stone, H. A.; Kim, S. *AIChE J.* **2001**, 47, 1250.

6 Haeberle, S.; Zengerle, R. *Lab Chip* **2007**, 7, 1094.

7 Toner, M.; Irimia, D. *Annu. Rev. Fluid Mech.* **2005**, 7, 77.

8 Erickson, D.; Li, D. *Anal. Chim. Acta* **2004**, 507, 11.

9 Pamme, N. *Lab Chip* **2007**, 7, 1644.

10 Dittrich, P. S.; Tachikawa, K.; Manz, A. *Anal. Chem.* **2006**, 78, 3887.

11 Yi, C.; Li, C. W.;Ji, S.;Yang, M. *Anal. Chim. Acta* **2006**, 560, 1.

12 Balasubramanian, A. K.; Soni, K. A.; Beskok, A.; Pillai, S. D. *Lab Chip* **2007**, 7, 1315.

13 Voldman, J.; Gray, M. L.; Toner, M.; Schmidt, M. A. *Anal. Chem.* **2002**, 74, 3984.

14 Lee, H.; Purdon, A. M.; Chu, V.; Westervelt, R. M. *Nano Lett.* **2004**, 4, 995.

15 Pamme, N.; Manz, A. *Anal. Chem.* **2004**, 76, 7250.

16 Wood, C. D.; Evans, S. D. *Appl. Phys. Lett.* **2008**, 92, 044104.

17 Wang, M. M.; Tu, E.; Raymond, D. E.; Yang, J. M.; Zhang, H.; Hagen, N.; Dees, B.; Mercer, E. M.; Forster, A. H.; Kariv, I.; Marchand, P. J.; Butler, W. F. *Nature Biotechnol.* **2005**, 23, 83.

18 Macdonald, M. P.; Spalding, G. C.; Dholakia, K. *Nature* **2003**, 426, 421.

19 Huang, L. R.; Tegenfelft, J. O.; Kraeft, J. J.; Sturm, J. C.; Austin, R. H.; Cox, E. C. *Nature Biotechnol.* **2002**, 10, 1048.

20 Pethig, R.; Markx, G. H. *Trends Biotechnol.* **1997**, 15, 426.

21 Wong, P. K.; Wang, T.-H.; Deval, J. H.; Ho, C.-M. *IEEE/ASME Trans. Mechatronics* **2004**, 9, 366.

22 Cheng, J.; Sheldon, E. L.; Wu, L.; Uribe, A.; Gerrue, L. O.; Carrino, J.; Heller, M. J.; O'Connell J. P. *Nature Biotechnol.* **1998**, 16, 541.

23 Gascoyne, P.; Mahidol, C.; Ruchirawat, M.; Satayavivad, J.; Watcharasit, P.; Beckera F. F. *Lab Chip* **2002**, 2, 70

24 Hughes, M. *Electrophoresis* **2002**, 23, 2569.

25 Kralj, J. G.; Lis, M. T. W.; Schmidt, M. A.; Jensen, K. F. *Anal. Chem.* **2006**, 78, 5019.

26 Rosenthal, A.; Voldman, J. *Biophys. J.* **2005**, 88, 2193.

27 Taff, B. M.; Voldman, J. *Anal. Chem.* **2005**, 77, 7976.

28 Gascoyne, P.; Vykoukal, J. *Electrophoresis* **2002**, 23, 1973.

29 Huang, Y.;Mather, E. L.; Bell, J. L.; Madou, M. *Anal. Bioanal. Chem.* **2002**, 372, 49.

30 Jones, T. B. *J. Electrostat.* **2001**, 51-52, 290.

31 Ramos, A.; Morgan, H.; Green, N. G.; Castellanos, A. *J. Phys. D: Appl. Phys.* **1998**, 31, 2338.

32 Aldaeus, F.; Lin, Y.; Roeraade, J.; Amberg, G. *Electrophoresis*, **2005**, 26, 4252.

33 Wang, X.-J.; Wang, X.-B.; Becker, F.F.; Gascoyne, P.R.C. *J. Phys. D: Appl. Phys.* **1996**, 29, 1649.

34 Morgan, H. A.; Izquierdo, G.; Bakewell, D.; Green, N.G.; Ramos, A. *J. Phys. D: Appl. Phys.* **2001** 34, 1553.

35 Green, N. G.; Ramos, A.; Morgan, H. *J. Electrostat.* **2002**, 56, 235.

36 Albrecht, D. R.; Sah, R. L.; Bhatia, S. N. *Biophys. J.* **2004**, 87,2131.

37 Erickson, D *Microfluid. Nanofluid.* **2005**, 1, 301.

38 Gagnon, Z.;Chang, H.-C. *Electrophoresis* **2005**, 26, 3725.

39 Tuval, I.; Mezic, I.; Bottausci F.; Zhang, Y. T.; MacDonald, N. C.; Piro, O. *Phys. Rev. Lett.* **2005**, 95, 236002.

40 Castellanos, A.; Ramos, A.; Gonz´alez, A.; Green, N. G.; Morgan, H. *J. Phys. D: Appl. Phys.* **2003**, 36, 2584.

41 Bahukudumbi, P.; Everett, W. N.;Beskok, A.; Bevan, M. A.; Huff, G. H.; Lagoudas, D.; Ounaies, Z. *Appl. Phys. Lett.* **2007**, 90, 224102.

42 Green, N. G.; Ramos, A.; Gonz´alez, A.; Morgan, H.; Castellanos, A. *Phys. Rev. E* **2000**, 61, 4011.

43 Gonz´alez. A,; Ramos, A.; Green, N. G.; Castellanos, A.; Morgan, H. *Phys. Rev. E* **2000**, 61, 4019.

44 Green, N. G.; Ramos, A.; Gonz´alez, A.; Morgan, H.; Castellanos, A. *Phys. Rev. E* **2002**, 66, 026305.

45 Ramos, A.; Morgan, H.; Green, N. G.; Castellanos, A. *J. Col. Int. Sci.* **1999**, 217, 420.

46 Morgan, H.; Green, N. G. AC Electrokinetics: Colloids and Nanoparticles; Research Studies Press: Hertfordshire, U. K., 2003.

47 Jones, T. B. Electromechanics of Particles; Cambridge University Press: Cambridge, U. K., 1995.

48 O'Brien, R. W. *J. Fluid Mech.* **1988**, 190, 71.

49 Green, N. G.; Morgan, H. *J. Phys. Chem. B* **1999**, 103, 41.

50 Bottcher, C. J. F. Theory of Electric Polarisation; Elsevier Press: London, 1952.

51 Lazcka, O.; Campo, F. D.; Munoz, F. X. *Biosens. Bioelectron.* **2007**, 22, 1205.

52 Rodriguez-Mozaz, S.; Marco, M. P.; LopezdeAlda, M. J.; Barcelo, D. *Anal. Bioanal. Chem.* **2004**, 378, 588.

53 Palchetti, I.; Mascini, M. *Anal. Bioanal. Chem.* **2008**, 391, 455.

54 Gascoyne, P.; Vykoukal, J. *Electrophoresis* **2002**, 23, 1973.

55 Voldman, J. *Annu. Rev. Biomed. Eng.* **2006**, 8, 425.

56 Zhou, R.; Wang, P.; Chang, H. C. *Electrophoresis* **2006**, 27, 1376.

57 Lapizco-Encinas, B. H.; Simmons, B. A.; Cummings, E. B.; Fintschenko, Y. *Electrophoresis* **2004**, 25, 1695.

58 Huang, Y.; Pethig, R. *Meas. Sci. Technol.* **1991**, 2, 1142.

59 Rosenthal, A; Taffa, B. M.;Voldman, J. *Lab Chip* **2006**, 6, 508.

60 Schnelle, T.; Muller, T.; Fuhr, G. *J. Electrostat.* **2000**, 50, 17.

61 Pethig, R.; Huang, Y.; Wang, X. B.; Burt, J. P. H. *J. Phys. D: Appl. Phys.* **1992**, 24, 881.

62 Bhatt, K. H.; Grego, S.;Velev, O. D. *Langmuir* **2005**, 21, 6603.

63 Suzuki, M.; Yasukawa, T.; Mase, Y.; Oyamatsu, D.;Shiku, H.; Matsue, T. *Langmuir* **2004**, 20, 11005.

64 Suzuki, M.; Yasukawa, T.; Shiku, H.; Matsue, T. *Langmuir* **2007**, 23, 4088.

65 Docoslis, A.; Espinoza, L. A. T.; Zhang, B.; Cheng, L.; Israel, B. A.; Alexandridis, P.; Abbott, N. L. *Langmuir* **2007**, 23, 3840.

66 Stevens, K. A.; Jaykus, L. *Crit. Rev. Microbiol.* **2004**, 30, 7.

67 Lim, D. V.; Simpson, J. M.; Kearns, E. A.; Kramer, M. F. *Clin. Microbiol. Rev.* **2005**, 18, 583.

68 Ermolina, I.; Morgan, H. *J. Col. Int. Sci.* **2005**, 285, 419.

69 Park, S.; Beskok, A. *Anal. Chem.* **2008**, 80, 2832.

70 Yeh, S. R.; Seul, M.; Shraiman, B. I. *Nature* **1997**, 386, 57.

71 Yethiraj, A. *Soft Matter* **2007**, 3, 1099.

72 Gonz´alez, A.; Ramos, A.; Morgan, H.; Green, N. G.; Castellanos, A. *J. Fluid Mech.* **2006**, 564, 415.

73 Green, N. G.; Ramos, A.; Gonzalez, A.; Castellanos, A; Morgan, H. *J. Electrostat.* **2001**, 53, 71.

74 Feldman, H. C.; Sigurdson, M.; Meinhart, C. D. *Lab Chip* **2007**, 7, 1553.

75 Lide, D.R. CRC Handbook of Chemistry and Physics 74th Edition; CRC Press: London, 1994.

76 Chen, D. F.; Du, H. *J. Micromech. Microeng.* **2006**, 16, 2411.

77 Lim, D. V.; Simpson, J. M.; Kearns, E. A.; Kramer, M. F. *Clin. Microbiol. Rev.* **2005**, 18, 583.

78 Stevens, K. A.; Jaykus, L. *Crit. Rev. Microbiol.* **2004**, 30, 7.

79 Wong, P. K.; Chen, C. Y.; Wang, T. H.; Ho, C. M. *Anal. Chem.* **2004**, 76, 6908.

80 Huang, Y.; Mather, E. L.; Bell, J. L.; Madou, M. *Anal. Bioanal. Chem.* **2002**, 372, 49.

81 Laurell, T.; Petersson, F.; Nilsson, A. *Chem. Soc. Rev.* **2007**, 36, 492.

82 Whitworth, G.; Coakley, W. T. *J. Acoust. Soc. Am*. **1992**, 91, 79.

83 Gor'kov, L. P. *Sov. Phys. Doklady* **1962**, 6, 773.

84 Spengler, J. F.; Coakley, W. T. *AIChE J.* **2003**, 49, 2773.

85 Coakley, W. T. *Trends Biotechnol.* **1997**, 15, 506.

86 Hawkes, J. J.; Coakley, W. T. *Sens. Actuators, B: Chem.* **2001**, 75, 213.

87 Lilliehorn, T.; Simu, U.; Nilsson, M.; Almqvist, M.; Stepinski, T.; Laurell, T.; Nilsson, J.; Johansson, S. *Ultrasonics* **2005**, 43, 293.

88 Nilsson, A.; Petersson, F.; Jonsson, H.; Laurell, T. *Lab Chip* **2004**, 4, 131.

89 Petersson, F.; Nilsson, A.; Jonsson, H.; Laurell, T. *Anal. Chem.* **2005**, 77, 1216.

90 Petersson, F.; Aberg, L.; Sward-Nilsson, A. M.; Laurell, T. *Anal. Chem.* **2007**, 79, 5117.

91 Evander, M.; Johansson, L.; Lilliehorn, T.; Piskur, J.; Lindvall, M.; Johansson, S.; Almqvist, M.; Laurell, T.; Nilsson, J. *Anal. Chem.* **2007**, 79, 2984.

92 Neild, A.; Oberti, S.; Dual, J. *Sens. Actuators, B: Chem.* **2007**, 121, 452.

93 Kamenetzky, E. A.; Magliocco, L. G.; Panzer, H. P. *Science* **1994**, 263, 207.

94 Park, S. H.; Xia, Y. *Langmuir* **1999**, 15, 266.

95 Scalora, M.; Dowling, J. P.; Bowden, C. M.; Bloemer, M. J. *Phys. Rev. Lett.* **1994**, 73, 1368.

96 Yablonovitch, E. *Phys. Rev. Lett.* **1987**, 58, 2059.

97 John, S. *Phys. Rev. Lett.* **1987**, 58, 2486.

98 Hynninen, A. P.; Thijssen, J. H. J.; Vermolen, E. C. M.; Dijkstra, M.; Blaaderen, A. V. *Nature Mater.* **2007**, 6, 202.

99 Haes, A. J.; Haynes, C. L.; McFarland, A. D.; Schatz, G. C.; Duyne, V. R. R.; Zou, S. L. *MRS Bull.* **2005**, 30, 368.

100 Kuncicky, D. M.; Prevo, B. G.; Velev, O. D. *J. Mater. Chem.* **2006**, 16, 1207.

101 Holland, B. T.; Blanford, C. F.; Stein, A. *Science* **1998**, 281, 538.

102 Johnson, S. A.; Ollivier, P. J.; Mallouk, T. E. *Science* **1999**, 283, 963.

103 Holtz, J. H.; Asher, S. A. *Nature* **1997**, 389, 829.

104 Holtz, J. H.; Holtz, J. S. W.; Munro, C. H.; Asher, S. A. *Anal. Chem.* **1998**, 70, 780.

APPENDIX

Bacterial spore sample preparation

Bacterial spore samples were provided from Dr. Suresh D. Pillai's group in Texas A&M University. The procedure for sample preparation is following: *C. sporogenes* (ATCC 3584) spores were obtained from vegetative cells inoculated into tubes with 10 ml of cooked meat medium, incubated at 37°C for 5 days under anaerobic conditions. Spores were harvested by centrifugation, washed six times (4,000 x g, 20 min, 4 °C) with distilled water to remove vegetative cell debris and stored at 4°C in 25 ml of 18 MΩ water until use. Microscopic observation confirmed that the final spore preparation was free of vegetative cells (< 5 % phase-dark spores). Direct microscopic counts of the spore suspensions were made in Petroff-Hausser counting chambers. One ml aliquots of *C. sporogenes* spore preparations containing ~10^8 spores/ml were stained with 3µl of a 1:1 mixture of SYTO9 and propidium iodide (LIVE/DEAD® BacLight™, Invitrogen) and incubated at room temperature for 30 minutes in the dark. The spores were centrifuged (10000 x g) for five minutes and the pellet was aseptically transferred to a clean container to avoid residual staining.

VITA

Seungkyung Park received his B.S. and M.S. degree in aerospace engineering from Korea Advanced Institute of Science and Technology (KAIST), South Korea in 1998 and 2000, respectively. His master's thesis was on development of numerical schemes for the simulation of two phase flow and cavitation phenomena. He worked as an associate research engineer at Hyundai Mobis, South Korea from 2000 to 2005. He started his Ph. D. program at Texas A&M University in Mechanical Engineering Department in 2005 under the supervision of Professor Ali Beskok. His research work is mainly focused on microfluidic technologies for biomedical lab-on-a-chip applications and material science.

He may be reached at Department of Mechanical Engineering, Texas A&M University, College Station, TX 77843-3123. His email is skp0405@tamu.edu.